



Cite this: *Energy Environ. Sci.*, 2025, 18, 10286

## Revealing ion storage mechanisms of high-entropy anode materials through element selection and structure design

Yuankai Huang, <sup>ab</sup> Meisheng Han, <sup>ab</sup> Hengyuan Hu, <sup>ab</sup> Zhiyu Zou, <sup>ab</sup> Kunxiong Zheng, <sup>ab</sup> Yongbiao Mu, <sup>ab</sup> Wenjia Li, <sup>ab</sup> Lei Wei, <sup>ab</sup> Lin Zeng <sup>ab</sup> and Tianshou Zhao <sup>ab</sup>

High-entropy materials (HEMs) have gained significant research interest as potential anodes for rechargeable ion batteries (RIBs), attributed to their exceptional electrochemical performance. However, the ion storage mechanisms in HEMs remain complex and incompletely understood, primarily due to multi-element synergy. This perspective critically examines the ion storage mechanisms of HEMs, focusing on intercalation, conversion, alloying, and the less-explored space charge. Emphasis is placed on the critical role of element selection in governing these mechanisms: anion elements are necessary for conversion reactions; Sn, Bi, Sb, Zn, In, Ge, and Si enable alloying, while transition metals like Fe, Co, and Ni are pivotal for space charge. Furthermore, we analyze the correlation among capacity, cycling stability, and fast-charging performance in HEMs relative to element selection. Elements promoting conversion, alloying, and space-charge mechanisms enhance capacity, whereas non-converting elements improve cycling stability. Anions with high electrical conductivity and cations facilitating space-charge formation improve fast-charging performance. We further emphasize that effective structural design is crucial to fully exploit these four mechanisms. The key principle is accelerating intercalation and conversion reaction kinetics, thereby promoting finer metal nanoparticle formation to maximize alloying and space-charge mechanisms. Finally, we outline current challenges and future research directions for HEM anodes in RIBs.

Received 18th September 2025,  
Accepted 21st October 2025

DOI: 10.1039/d5ee05507e

rsc.li/ees

### Broader context

The growing demand for high-energy-density rechargeable ion batteries drives the rapid development of high-entropy materials (HEMs) that synergistically integrate multiple ion storage mechanisms—intercalation, conversion, alloying, and space-charge storage—within a single electrode system. This perspective systematically elucidates the intrinsic characteristics and synergistic interactions of the four core ion-storage mechanisms in HEM anodes, demonstrating how strategic element selection (including cation/anion zoning) and tailored structural design (*e.g.*, multi-mechanism enabling nano-architectures) collectively enhance specific capacity, cycling lifespan, and fast-charging performance. Furthermore, we identify key future research directions: AI-driven design for optimizing HEM compositions and structures, atomic-level multi-scale structural control, and *in situ/operando* characterization techniques to quantify four mechanism contributions on capacity. Collectively, this perspective provides a comprehensive framework essential for developing high-performance HEM anodes for next-generation RIBs, though their widespread deployment remains subject to overcoming synthesis and manufacturing bottlenecks related to multi-element precision, cost, and process control.

## 1. Introduction

Rechargeable ion batteries (RIBs) have become the cornerstone technology for efficient bidirectional conversion between

electrical and chemical energy due to their high energy density, good fast-charging, and long cycle life.<sup>1,2</sup> This capability provides essential support for the use of portable electronic devices, the realization of electrification of transportation, and the large-scale deployment of renewable energy. Among current technologies, lithium-ion batteries (LIBs), leveraging their well-established industrial foundation, have secured a dominant position in the consumer electronics sector and are making significant inroads into the electric vehicles and electric vertical take-off and landing market.<sup>3</sup> Meanwhile, sodium-

<sup>a</sup> Shenzhen Key Laboratory of Advanced Energy Storage, Department of Mechanical and Energy Engineering, Southern University of Science and Technology, Shenzhen 518055, China. E-mail: hanms@sustech.edu.cn, zhaots@sustech.edu.cn

<sup>b</sup> SUSTech Energy Institute for Carbon Neutrality, Southern University of Science and Technology, Shenzhen 518055, China

ion batteries (SIBs), leveraging the abundance of sodium resources, inherent cost advantages, and excellent low-temperature and fast-charging performance, demonstrate considerable promise for large-scale energy storage applications and electric vehicles.<sup>4</sup> Furthermore, emerging RIB systems based on K, Ca, Mg, *etc.* are continuously pushing the technological boundaries, collectively enabling a multi-tiered energy storage ecosystem.<sup>5–7</sup> Fundamentally, battery operation relies on directional ion migration through electrolytes and redox reactions at electrode interfaces during charge/discharge cycles. Within this framework, the anode serves as the primary host for ion intercalation/deintercalation, making its performance critical for key battery metrics.<sup>8</sup> Crucially, the ion storage mechanisms fundamentally dictate the anode materials' capacity, fast-charging performance, and cyclability.

Based on distinct ion storage mechanisms, anode materials are primarily categorized into four major systems: intercalation (*e.g.*, graphite,  $\text{Li}_4\text{Ti}_5\text{O}_{12}$ , *etc.*), conversion (*e.g.*, transition metal oxides, phosphides, sulfides, *etc.*), alloying (*e.g.*, Si, Sn, and Ge), and space charge.<sup>9,10</sup> Intercalation-type materials store energy through the reversible insertion/extraction of ions into/from lattice interstices or interlayer spaces (Fig. 1a). Renowned for their low volume strain and high structural stability, they represent the mainstream commercial anode choice for RIBs. However, they face challenges such as limited theoretical capacity or poor intrinsic conductivity.<sup>11</sup> Conversion-type materials achieve high specific capacity through the reversible breaking/reformation of chemical bonds (Fig. 1b). Nevertheless, they are hindered by sluggish reaction kinetics, significant volume effects, and insufficient conductivity. Performance optimization often necessitates nanocrystalline design, carbon compositing, and defect engineering to achieve enhanced reaction dynamics.<sup>12,13</sup> Alloying-type materials deliver ultra-high capacity *via* alloying reactions (Fig. 1c), but suffer from severe volume expansion leading to electrode pulverization. Strategies like nano-structuring, porous structure, carbon compositing, or incorporating oxide buffers are employed to mitigate stress.<sup>14</sup> Particularly noteworthy are recent findings

revealing an additional ion storage mechanism in conversion-type anodes during low-voltage discharge: metal salt crystals produced by the conversion reaction can further store charged ions. This occurs through the injection of spin-polarized electrons into the metal nanoparticle ( $\text{M}^0$ ) surface, and the corresponding cations are stored in the bulk phase of the metal salt. Simultaneously, a space-charge region forms at grain boundaries while magnetization undergoes a significant reduction (Fig. 1d).<sup>15,16</sup>

High-entropy materials (HEMs) originate from the concept of high-entropy alloys proposed by Cantor *et al.*<sup>17</sup> and Yeh *et al.*<sup>18</sup> They are formed by integrating five or more elements in equimolar or near-equimolar ratios (composition range: 5–35 at%) into a single-phase crystalline structure characterized by configurational disorder. Their unique physical, mechanical, and electrochemical properties stem from four core effects: high-entropy effect (stabilizing solid-solution phases), severe lattice distortion (stress field reconstruction due to atomic size mismatch), sluggish diffusion (inhibiting phase transformations), and the cocktail effect (synergistic multi-element modulation of an electronic structure).<sup>19</sup> This design strategy has been extended to diverse systems, including high-entropy oxides,<sup>20</sup> sulfides,<sup>21</sup> phosphides,<sup>22</sup> fluorophosphates,<sup>23</sup> and borides,<sup>24</sup> finding broad application in electrochemical energy storage. Critically, the elemental diversity of HEMs enables the concurrent operation of multiple energy storage mechanisms—including intercalation, conversion, alloying, and space charge. This multi-mechanism synergy facilitates a triple breakthrough: capacity multiplication by superimposing reaction pathways to transcend the limits of single mechanisms; kinetics optimization *via* vacancy and dislocation introduction through defect engineering; and structural self-stabilization achieved by suppressing volumetric degradation through differentiated stress distribution. By leveraging this multi-mechanism synergy, HEM anodes enable the integration of high capacity, long cycle life, and fast-charging capability, thereby laying the material foundation for next-generation energy storage devices.

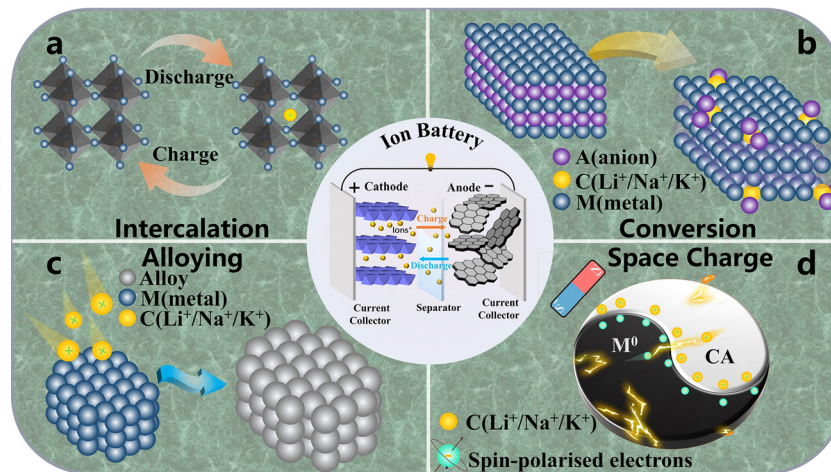


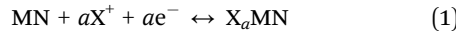
Fig. 1 Ion storage mechanisms of RIBs anodes: (a) intercalation, (b) conversion, (c) alloying, and (d) space charge.

Recently, HEMs have stimulated significant research interest as anodes for RIBs. It is noteworthy that the working potential and underlying charge storage mechanisms differ significantly between cathodes and anodes.<sup>19</sup> Cathodes typically operate at relatively high potentials and often rely on reversible cationic and/or anionic redox reactions in insertion-type frameworks.<sup>25</sup> In contrast, anode materials function at lower potentials, which enable the involvement of a broader spectrum of ion storage mechanisms, including intercalation, conversion, alloying, and space charge.<sup>16,20-24</sup> While several reviews on HEM anodes exist, they largely concentrate on defining HEMs, and discussing their synthesis routes and applications.<sup>26-28</sup> A comprehensive overview and future perspective, specifically on the ion storage mechanisms of HEM anodes, are particularly scarce, as are comprehensive reviews addressing critical determinants such as element selection and structure design. This perspective offers a comprehensive analysis of the four ion storage mechanisms—intercalation, conversion, alloying, and space charge—in HEM anodes. Furthermore, it offers a forward-looking analysis on how synergistic element selection and structure design collaboratively influence the four mechanisms, thus enhancing electrochemical performances. By elucidating the multi-scale mechanisms coupling in HEM anodes, this perspective aims to reveal the underlying “composition–structure–property” relationship and establish a novel paradigm for overcoming the capacity, cycling life, and fast-charging limitations of conventional anode materials in RIBs.

## 2. Four core ion storage mechanisms

### 2.1. Intercalation

The process of introducing external ions into a host lattice is termed “intercalation”. As shown in eqn (1), intercalation reactions occur within electrode materials  $MN$  (where  $M = Fe, Co, Ni, Mn, Cu, etc.$ , and  $N = O, S, P, Se, etc.$ ), incorporating alkali metal ions ( $X = Li, Na, or K$ ) to form the intercalation compound  $X_aMN$ . During this process, the structure of the guest–host compound undergoes only minimal changes compared to the host structure. Due to an extremely low degree of volume change caused by intercalation reactions in the material lattice, intercalation-type electrodes typically exhibit exceptional cycling stability.<sup>29</sup> Furthermore, the intercalation/deintercalation process is reversible. Intercalation reactions induce controlled and systematic modifications to the physical properties of the host lattice, particularly its electronic, magnetic, and optical characteristics.<sup>30</sup>

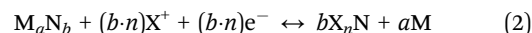


The intercalation mechanisms in high-entropy anode materials have been extensively investigated. In 2021, Huang *et al.*<sup>31</sup> utilized transmission electron microscopy (TEM) and electron energy-loss spectroscopy (EELS) to characterize the lithium intercalation process in high-entropy spinel oxide  $(CrMnFeCo-Ni)_3O_4$  (Fig. 2a). During this process, Mn tends to segregate

from other elements during cycling, leading to the formation of  $Cr_xFe_{3-x}O_4$  phases in Fe/Cr-rich regions (Fig. 2b–f). Conversely, Ni/Co-rich regions further react with intercalated Li ions to form  $LiNi_xCo_{1-x}O_2$  phases. The EELS spectra of Cr, Mn, Fe, Co, and Ni acquired during cycling show high similarity between the spectra obtained in the first and second lithiation steps, as well as between those obtained after the first and second delithiation steps. These results indicate highly reversible changes in the valence states of elements within the HEO electrode. Furthermore, the  $LiNi_xCo_{1-x}O_2$  phase generated by the intercalation reaction remains persistent throughout the lithiation/delithiation cycles. This persistent phase acts as a structural stabilizer, contributing to the exceptional electrode cyclability. Subsequently, Zhao *et al.*<sup>32</sup> employed high-resolution TEM to observe the intercalation reaction process in the high-entropy anode material  $CuMnFeSnGeS$  for SIBs (Fig. 2g–j). HRTEM images discharged to 0.6 V clearly reveal the (020) lattice planes of  $Na_xCuMnFeSnGeS$  (Fig. 2g), indicating the intercalation of  $Na^+$  into  $CuMnFeSnGeS$ . Ultimately, upon charging to 3.0 V, the reappearance of the (220) planes of  $CuMnFeSnGeS$  is clearly visible in Fig. 2j, demonstrating highly reversible sodium storage performance. Similarly, Chien *et al.*<sup>33</sup> investigated the potassium-ion storage mechanism in the high-entropy anode  $CoV-MnFeZnPS_3$  for potassium-ion batteries (PIBs) (Fig. 2k–s), also revealing its high reversibility during charging and discharging. Currently reported high-entropy anode materials for various RIBs—encompassing oxides, chalcogenides, phosphides, and alloy systems incorporating transition metals, alkaline earth metals, and main group metals—all involve the intercalation reaction mechanism.<sup>9,31-39</sup> Notably, Cheng *et al.*<sup>40</sup> revealed that in high-entropy anodes, the intercalation reaction primarily occurs during the early stages of discharge (low depth of discharge), and its contribution to the sodium storage capacity significantly diminishes upon further discharge.

### 2.2. Conversion

The conversion reaction constitutes a distinct energy storage mechanism in advanced electrode materials, defined by the complete reconstruction of the host material's chemical bonding network. Unlike intercalation reactions—which involve reversible ion insertion/extraction without breaking primary bonds—conversion reactions entail the full cleavage of the host's original chemical bonds. Consequently, the theoretical capacity can reach 3–5 times that of intercalation materials. Furthermore, unlike intercalation, the metallic elements ( $M$ ) generated *via* conversion reactions can potentially exhibit even greater capacities through subsequent alloying or space-charge mechanisms.<sup>10,16,21</sup> In HEMs, conversion reactions often occur concomitantly with intercalation. Here, the electrochemically active metal compounds ( $M_aN_b$ ) can react with ions ( $X^+$ ), transforming into metallic elements ( $M$ ) and Li/Na/K salts ( $X_nN$ ) as described in eqn (2).<sup>35,41,42</sup>



Research studies on the conversion reaction mechanisms of HEMs in RIBs have rapidly emerged in recent years. This surge

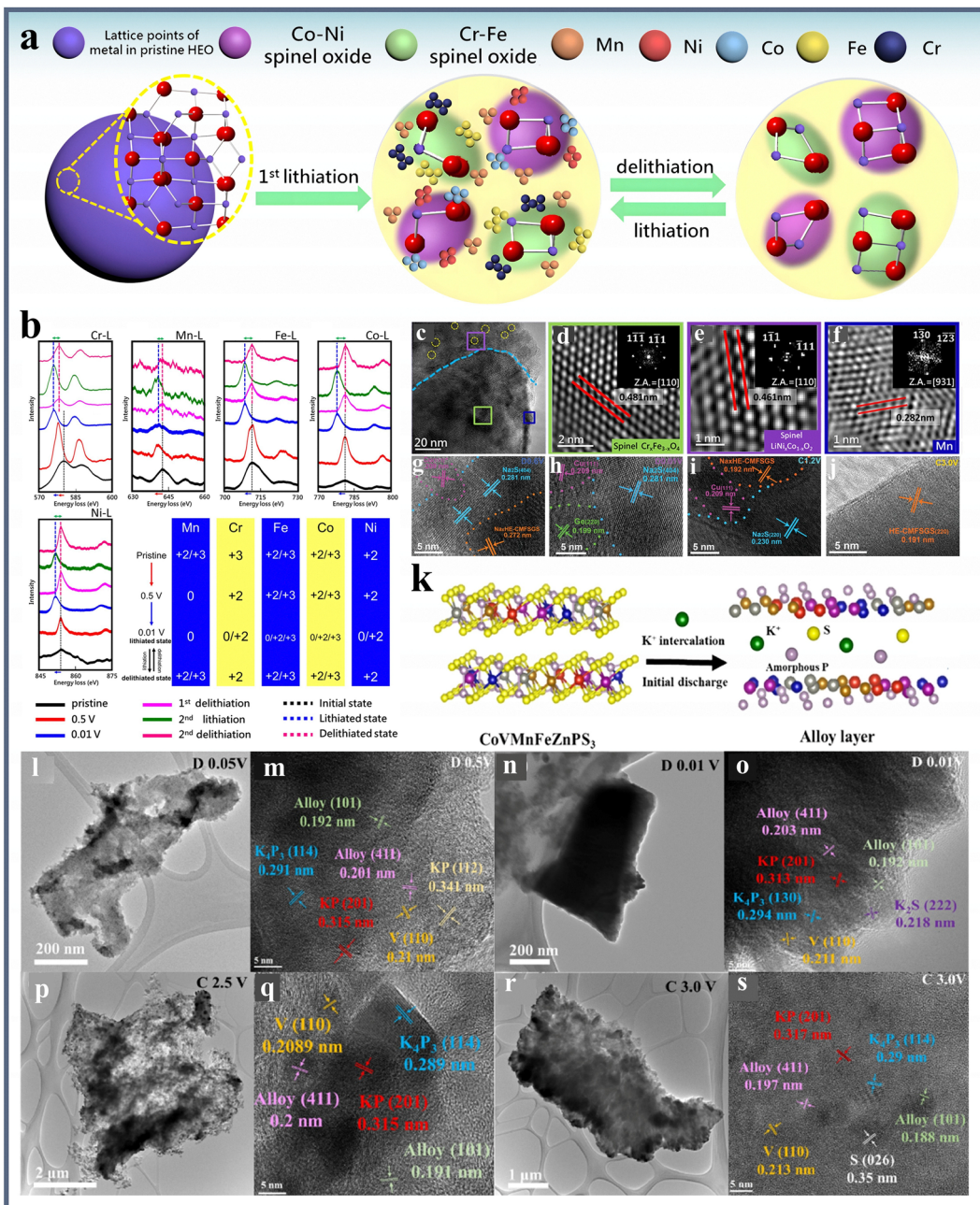


**Fig. 2** (a) Lithiation/delithiation processes in  $(\text{CrMnFeCoNi})_3\text{O}_4$ , and (b) EELS L-edge spectra of Cr, Mn, Fe, Co, and Ni elements and summary of valence state variations of constituent elements of HEO. (c) TEM and HRTEM images of (d)  $\text{Cr}_x\text{Fe}_{3-x}\text{O}_4$ , (e)  $\text{LiNi}_{1-x}\text{Co}_{1-x}\text{O}_2$ , and (f) Mn phases of  $(\text{CrMnFeCoNi})_3\text{O}_4$ . Reproduced with permission.<sup>31</sup> Copyright 2021, Elsevier Inc. *Ex situ* TEM patterns under sodiation conditions of  $\text{CuMnFeSnGeS}$  at (g) 0.6 V and (h) 0.01 V and desodiation states of (i) 1.2 V and (j) 3.0 V. Reproduced with permission.<sup>32</sup> Copyright 2022, Wiley-VCH. (k) Schematic illustration of the  $\text{K}^+$  storage mechanism  $\text{CoVMnFeZnPS}_3$  during the charging/discharging process. Low magnification TEM images of the cycled  $\text{CoVMnFeZnPS}_3$ : (l) and (m) discharged to 0.05 V, (n) and (o) discharged to 0.01 V, (p) and (q) charged to 2.5 V, and (r) and (s) charged to 3.0 V. Reproduced with permission.<sup>33</sup> Copyright 2023, Elsevier Inc.

is driven by the dual advantages arising from synergistic effects among multiple active sites: breakthrough improvements in theoretical capacity and unique structural buffering capabilities. Liu *et al.*<sup>41</sup> utilized selected-area electron diffraction (SAED) and *in situ* X-ray diffraction (XRD) to characterize the conversion reaction process in  $(\text{LiFeZnNiCoMn})_3\text{O}_4$  serving as a LIB anode (Fig. 3a). The SAED and XRD results reveal that the

emergence of diffraction rings corresponding to Fe, Co, Ni, and  $\text{Li}_2\text{O}$ , alongside the disappearance of diffraction peaks of the spinel phase, signifies the occurrence of the conversion reaction (Fig. 3b-h). Furthermore, upon full charging, the diffraction rings for Fe, Co, Ni, and  $\text{Li}_2\text{O}$  progressively become invisible, with only the diffraction patterns of the parent spinel and rock-salt phases being identified, confirming the high

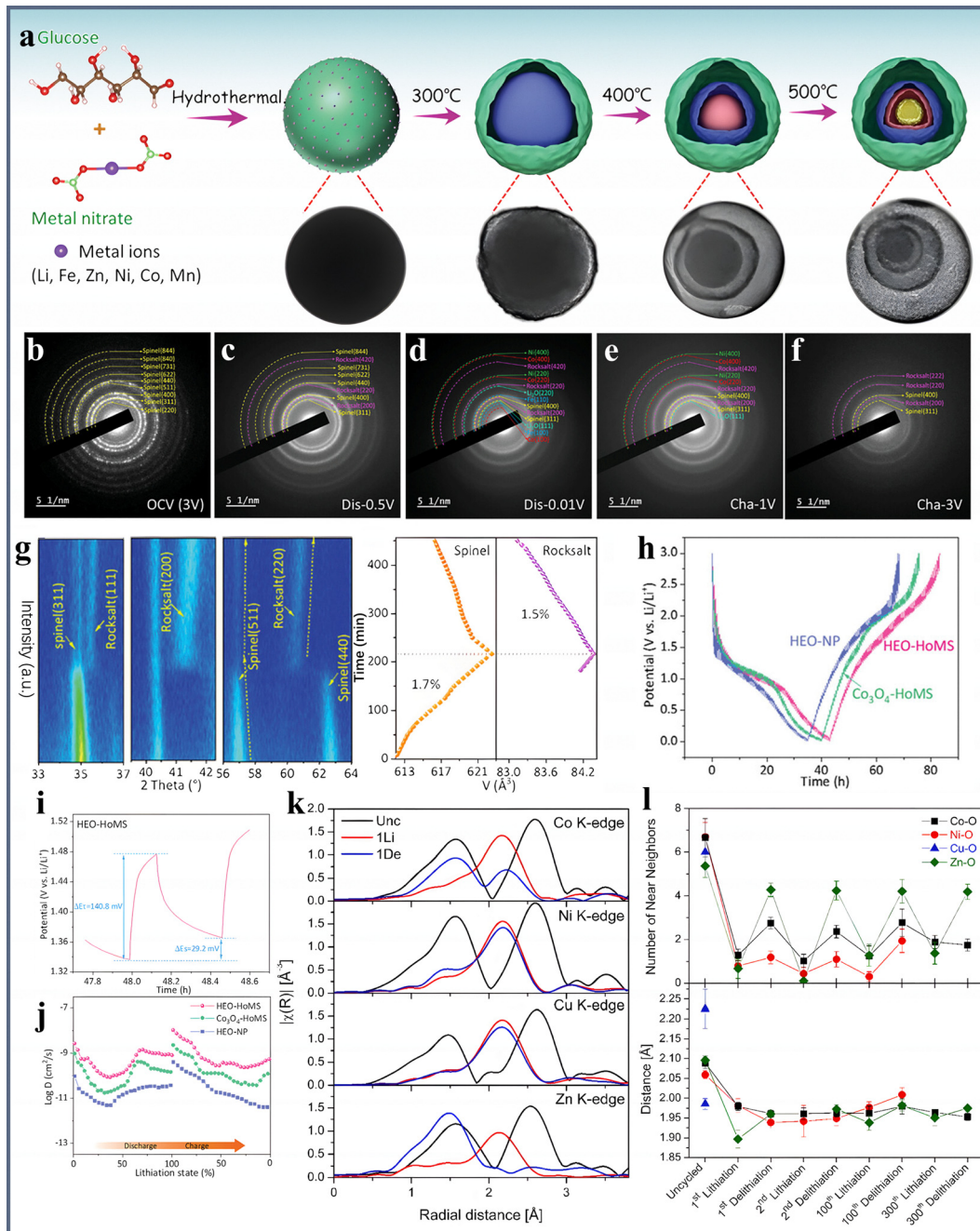


**Fig. 3** (a) Schematic diagram of morphology evolution of  $(\text{LiFeZnNiCoMn})_3\text{O}_4$ . (b)-(f) SAED patterns at different voltages for identifying phase evolution. (g) *In situ* XRD patterns, contour maps, and cell volume variations of the  $(\text{LiFeZnNiCoMn})_3\text{O}_4$  electrode upon first cycling. (h) GITT curves of different electrodes. (i) Enlarged GITT curve of  $(\text{LiFeZnNiCoMn})_3\text{O}_4$ -HoMS. (j) The calculated  $\text{Li}^+$  diffusion coefficients of different electrodes. Reproduced with permission.<sup>41</sup> Copyright 2024, Wiley-VCH. (k) Fourier transforms of the EXAFS spectra of Co, Ni, Cu and Zn K-edges at uncycled (black), 1st lithiated (red), and 1st delithiated (blue) states. (l) EXAFS fit results: number of near neighbors (top) and TM-O distance (bottom) for Co-O (black square), Ni-O (red circle), Cu-O (blue triangle), and Zn-O (green diamond) as a function of charging states. Reproduced with permission.<sup>46</sup> Copyright 2023, Elsevier Inc.

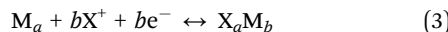
reversibility of conversion reactions within the electrode. Additionally, galvanostatic intermittent titration technique (GITT) analysis confirms a high  $\text{Li}^+$  diffusion coefficient in the  $(\text{LiFeZnNiCoMn})_3\text{O}_4$ -HoMS material (Fig. 3i-k). Notably, the  $\text{Li}_2\text{O}$  matrix generated by the conversion reaction provides shortcut pathways for ion conduction, resulting in the fastest  $\text{Li}^+$  diffusion observed in the fully lithiated state. Research demonstrates that

the conversion reaction exhibits universality in the energy storage field and is not confined to oxide anodes in LIBs. This mechanism has also been validated in HEM anodes for SIBs/PIBs across diverse compound systems, including oxides, sulfides, selenides, phosphides, and tellurides, incorporating a wide range of elements such as transition metals, main group metals, and noble metals.<sup>32,33,43-45</sup> However, the conversion process from metal

compounds to metallic phases involves multi-electron transfer, triggering the cleavage and reformation of chemical bonds, which inevitably leads to lattice collapse and drastic volume expansion. Resolving this fundamental conflict is a key challenge for advancing practical applications. Specifically, the reversibility of conversion reactions in high-entropy anodes exhibits significant disparities. Microstructural heterogeneity causes discrete energy barriers for bond reformation, inducing irreversible phase separation. Meanwhile, the entropy stabilization effect can only delay, but not entirely prevent, the structural collapse resulting from chemical bond cleavage, ultimately resulting in poor cyclic stability. Marques *et al.*<sup>46</sup> confirmed this mechanism through Fourier transforms and fitting results of the extended X-ray absorption fine structure (EXAFS) spectra. For  $(\text{Mg}_{0.2}\text{Co}_{0.2}\text{Ni}_{0.2}\text{Cu}_{0.2}\text{Zn}_{0.2})\text{O}$ , during the conversion/de-conversion process, only partial re-oxidation occurs for Co and Ni, while Zn undergoes complete oxidation. Crucially, only Zn maintains reversible conversion behavior after long-term cycling (300 cycles) (Fig. 3l and m).

### 2.3. Alloying

Beyond intercalation and conversion, alloying constitutes another chemically distinct mechanism for alkali-ion storage. During the alloying process, alkali metal ions form intermetallic compounds with host metals or semimetals from Group IV and V elements (eqn (3)). Si, Sb, Ge, Bi, and Sn are recognized as common base materials for alloying reactions.<sup>9</sup> Distinct from intercalation reactions involving only ion insertion, this process entails chemical bond reconstruction, where alkali metal atoms embed into the metal lattice, forming new phases with covalent/metallic bonding. Nevertheless, alloying reactions based on non-Group IV/V metals (e.g., In and Zn) in HEM anodes have also been reported.<sup>44,47–49</sup>



Alloying reactions often coexist with intercalation and conversion reactions, enabling anode materials with low Li/Na/K insertion potentials to achieve exceptionally high specific capacities far exceeding those of single-mechanism materials. Li *et al.*<sup>47</sup> investigated the alloying reactions of In, Ge, and Si in the InGeSiP<sub>3</sub> LIB anode material during deep discharge, along with the synergistic effects among intercalation, conversion, and alloying reactions, using *in situ* XRD (Fig. 4a). This concept is subsequently extended to HEMs such as GaCuZnInGeSiP<sub>6</sub>, GaCu(or Zn)InGeSiP<sub>5</sub>, and CuZnInGeSiP<sub>5</sub>. Nevertheless, severe volume expansion induced by alloying reactions remains a key challenge for anodes, as particle pulverization and interfacial instability accelerate capacity degradation. HEMs address this issue synergistically through a trinity mechanism: an entropy-stabilization-induced lattice distortion network disperses stress; a “cocktail” effect optimizes the reaction sequence to delay stress concentration; and interfacial self-adaptivity dynamically maintains ionic channel integrity.<sup>35,36,50–52</sup> This enables reversible alloying reactions even in SIBs and PIBs with larger ionic radius, achieving exceptional capacity and

cycling stability. Wang *et al.*<sup>44</sup> synthesized a high-configuration-entropy  $\text{Sb}_{1.4}\text{Bi}_{0.2}\text{Sn}_{0.2}\text{Co}_{0.1}\text{Mn}_{0.1}\text{Te}_3$  anode for PIBs. As shown in Fig. 4b, polycrystalline diffraction rings from the (420) plane of cubic  $\text{K}_3\text{Sb}$ , the (220) plane of cubic  $\text{K}_3\text{Bi}$ , and the (745) plane of tetragonal  $\text{KSn}$ , along with HRTEM lattice fringes—specifically the (220) plane of cubic  $\text{K}_3\text{Sb}$  along the  $[1\bar{1}\bar{1}]$  zone axis, the (400) plane of cubic  $\text{K}_3\text{Bi}$  along the  $[0\bar{1}\bar{1}]$  zone axis, and the (321) plane of tetragonal  $\text{KSn}$  along the  $[1\bar{2}\bar{1}]$  zone axis—collectively confirm alloying reactions in  $\text{Sb}_{1.4}\text{Bi}_{0.2}\text{Sn}_{0.2}\text{Co}_{0.1}\text{Mn}_{0.1}\text{Te}_3$ . Similarly, Zhang *et al.*<sup>49</sup> used HRTEM to identify lattice fringes corresponding to alloying products ( $\text{Na}_9\text{Sn}_4$ ,  $\text{Na}_3\text{Sb}$ , and  $\text{Na}_3\text{Bi}$ ) in the hexagonal  $\text{Cu}_{0.88}\text{Sn}_{0.02}\text{Sb}_{0.02}\text{Bi}_{0.02}\text{Mn}_{0.02}\text{S}_{0.9}\text{Se}_{0.1}$  high-entropy SIB anode (Fig. 4c–e), directly demonstrating the synergistic conversion-alloying sodium storage mechanism in HEMs. Furthermore, the reversible restoration of lattice fringes in  $\text{Cu}_{0.88}\text{Sn}_{0.02}\text{Sb}_{0.02}\text{Bi}_{0.02}\text{Mn}_{0.02}\text{S}_{0.9}\text{Se}_{0.1}$  upon complete desodiation confirms the reversibility of this coupled mechanism.

### 2.4. Space charge

Transition metal salts often show substantially higher capacities than their theoretical capacity calculated based on intercalation, conversion, and alloying. The intrinsic mechanisms behind their anomalous capacities exceeding theoretical limits remain a subject of ongoing debate in academia.<sup>53</sup> In 2002, Laruelle *et al.*<sup>54</sup> proposed a potential correlation between the extra electrochemical capacity in metal oxide LIBs and the growth of a polymeric or gel-like film surrounding transition metal ( $\text{M}^0$ ) nanoparticles within the low discharge voltage window. Voltage-window cycling is applied to confine the electrochemical operation to specific potential ranges, thereby isolating the extra capacity exclusively to the low-voltage region where the film forms and establishing its potential-dependent nature. *Ex situ* TEM observation directly correlates the film's appearance and disappearance with the charge–discharge states, visually confirming its reversible formation and dissolution were synchronized with the extra capacity, thus providing definitive structural evidence. Kinetic analysis *via* cyclic voltammetry (CV) characterizes the current response as a function of scan rate, which demonstrated a capacitive-like (as opposed to diffusion-limited) behavior, confirming the pseudocapacitive charge storage mechanism of the surface film. Subsequent studies have elucidated the mechanism of interfacial space-charge storage, wherein in transition metal oxide anode materials, excess Li ions are accommodated within the  $\text{Li}_2\text{O}$  bulk phase formed during conversion, while electrons accumulate at the metallic phase, collectively establishing a space-charge layer that contributes additional capacity.<sup>10,55</sup> This space-charge-derived capacity is clearly distinguishable from other sources of excess capacity. The space-charge capacity is intrinsically interface-driven, arising from localized charge separation at the  $\text{Li}_2\text{O}$ /metal interfaces, which can be measured using *operando* magnetometry. It also differs fundamentally from surface adsorption, which relies on a finite number of immobilized surface sites for charge trapping—lacking cross-phase electron compensation—and often leads to irreversible capacity saturation. By contrast, space-charge storage involves  $\text{Li}^+$  insertion

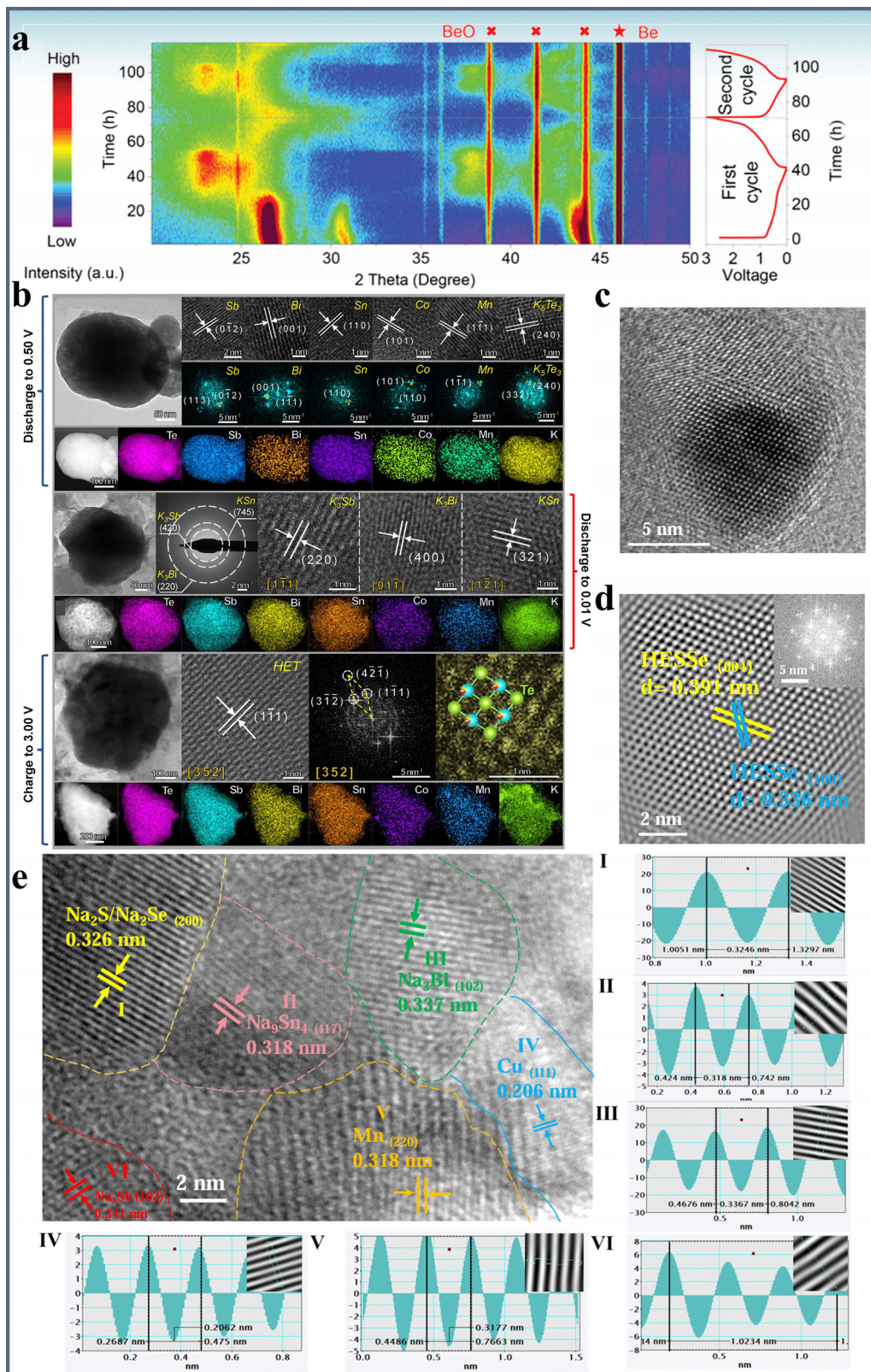


**Fig. 4** (a) *In situ* XRD along with the GCD profiles of InGeSiP<sub>3</sub>. Reproduced with permission.<sup>47</sup> Copyright 2024, Wiley-VCH. (b) TEM image, IFFT patterns, and SAED pattern of Sb<sub>1.4</sub>Bi<sub>0.2</sub>Sn<sub>0.2</sub>Co<sub>0.1</sub>Mn<sub>0.1</sub>Te<sub>3</sub> when charging and discharging. Reproduced with permission.<sup>44</sup> Copyright 2025, American Chemical Society. (c)–(e) HRTEM images for the Cu<sub>0.88</sub>Sn<sub>0.02</sub>Sb<sub>0.02</sub>Bi<sub>0.02</sub>Mn<sub>0.02</sub>S<sub>0.9</sub>Se<sub>0.1</sub> electrode at 0.1 V and (I–VI) corresponding intensity profiles and fast Fourier transform (FFT) pattern; HRTEM images of 3.0 V states and corresponding FFT patterns. Reproduced with permission.<sup>49</sup> Copyright 2025, Nature Publishing Group.

into  $\text{Li}_2\text{O}$  and electron localization in the metal phase, reversibly coupled *via* the interfacial electric field without site saturation, thereby enabling stable cycling.<sup>16</sup> Moreover, unlike irreversible electrolyte decomposition—which continuously consumes active lithium through parasitic reactions, forms electrochemically inert species, and leads to progressive capacity fading with low coulombic efficiency, as can be detected using isotope labeling techniques<sup>56</sup>—the space-charge contribution demonstrates exceptional reversibility and cycling stability. This mechanism operates through electrostatic accumulation at metal– $\text{Li}_2\text{O}$  interfaces without involving chemical breakdown of electrolyte components or generating persistent surface films, thereby fundamentally distinguishing it from capacity derived from side reactions.<sup>55</sup>

In 2020, Li *et al.*<sup>57</sup> employed *operando* magnetometry to investigate the origin of “extra capacity” and the evolution of the internal electronic structure in  $\text{Fe}_3\text{O}_4/\text{Li}$  cells. They concluded that the formation of the space-charge zone is the primary source of extra capacity in the  $\text{Fe}_3\text{O}_4/\text{Li}$  system. The formation mechanism is as follows: the accumulation of spin-polarized charges within the first few atomic layers at metal–insulator interfaces can induce significant changes in interfacial magnetization, governed by the surface density of states and near-Fermi-level spin polarization of the ferromagnetic metal.<sup>58</sup> In 3d transition metals, ferromagnetism originates from differential filling of majority- and minority-spin d-bands, where the majority-spin up ( $\uparrow$ ) d-band exhibits substantially higher occupancy than the minority-spin down ( $\downarrow$ ) counterpart (Fig. 5a). Net magnetization intensity ( $M$ ) is given by  $M = (N_{\uparrow} - N_{\downarrow})\mu_{\text{B}}$ , where  $N_{\uparrow}$  and  $N_{\downarrow}$  are the total number of electrons in each spin, and  $\mu_{\text{B}}$  is the Bohr magneton. It is proposed that spin-polarized charge storage ( $Q^s$ , in  $\text{mAh g}^{-1}$ ) correlates with extra charge storage ( $Q^{\text{extra}}$ ) provided by surface capacitance *via* effective spin polarization ( $P$ ) (eqn (4)). Neglecting minor orbital angular momentum contributions, each additional electron contributes a magnetic moment of +1 or -1 Bohr magneton, depending on which spin band it occupies. Consequently, the net change in surface magnetization  $\Delta M$  under high magnetic fields depends on the accumulation of spin-polarized electrons (with elementary charge  $e$ ) at the Fermi surface, as expressed in eqn (5). Based on this equation, the capacity contribution values of space-charge effects can be estimated from magnetization variations. During low-potential discharge (0.01–1 V), the  $\text{Fe}_3\text{O}_4$  electrode exhibits a rectangular CV profile. Power-law analysis ( $i = av^b$ ) yields a  $b$ -value of 1 for both anodic and cathodic peaks, confirming capacitive behavior dominates in the low-voltage region. This capacitive process demonstrates high reversibility, as evidenced by magnetic response measurements: magnetization decreases substantially during discharge and fully recovers upon charging. This directly demonstrates the excellent reversibility of the spin-polarized capacitive reaction occurring at the  $\text{Fe}^0/\text{Li}_2\text{O}$  interfaces. Specifically, as depicted in Fig. 5b, during low-potential discharge at the  $\text{Fe}^0/\text{Li}_2\text{O}$  interfaces, spin-polarized electrons are injected into the d orbitals of the Fe to a depth comparable to the

Thomas–Fermi screening length, and the corresponding Li ions are stored in the  $\text{Li}_2\text{O}$ , forming a space-charge zone.

$$Q^s = P \times Q^{\text{extra}} \quad (4)$$

$$\Delta M = \frac{3.6 \times Q^s}{e} \times \mu_{\text{B}} = \frac{3.6 \times Q^{\text{extra}}}{e} \times P \times \mu_{\text{B}}. \quad (5)$$

With further research, the space-charge effect has extended beyond LIBs and transition metal oxide systems to SIBs and sulfur/selenium compounds, emerging as a universal mechanism for ion storage. Li *et al.*<sup>59</sup> discovered a marked decrease in magnetization during discharge (highlighted in “region 3” of Fig. 5c) within the low-voltage range of 0.8–0.01 V for the  $\text{FeS}/\text{Li}$  system *via* *operando* magnetometry, followed by a subsequent increase during charging (0.01–1.6 V). This confirms ion–electron decoupling storage, where Fe acts as the electron acceptor phase and  $\text{Li}_2\text{S}$  as the  $\text{Li}^+$  acceptor phase—termed the “job-sharing” mechanism—providing additional battery capacity. Further investigation during low-potential discharge (0.01–1.2 V) successfully measures the rectangular profile in CV curves and reversible magnetic variations (Fig. 5d and e). Qiu *et al.*,<sup>60</sup> through *ex situ* M–H curve studies and discharge curve fitting for FeSe nanosheets in the low-voltage region, found that although FeSe nanosheets exhibit surface sodium storage behavior, their magnetic moment continuously increases in this region (Fig. 5f). This phenomenon contradicts the conventional electric double-layer mechanism. The slopes of the  $F(Q, E)$  vs.  $Q$  curves match the expected magnitudes (Fig. 5g), further confirming a space-charge sodium storage mechanism involving superparamagnetic  $\text{Fe}^0$  nanoparticles: spin-polarized electrons inject into the d-orbitals of  $\text{Fe}^0$ , while  $\text{Na}^+$  ions enter the  $\text{Na}_2\text{Se}$  bulk phase. Ultimately, an “intercalation-conversion-space charge” sodium storage mechanism for FeSe nanosheets is established (Fig. 5h).

Notably, existing studies have confirmed that the space-charge effect—which plays a positive role in balancing high capacity and rate performance—exists in transition metal (*e.g.*, Fe and Co) compounds for both LIBs and SIBs, spanning oxides, sulfides, selenides, and oxysalts (such as hydroxides and carbonates).<sup>57,59–62</sup> Furthermore, our recent experimental result, revealed by *operando* magnetometry (Fig. 5i), shows that the formed Ni nanoparticles during conversion can also trigger a space-charge storage mechanism in  $\text{NiS}/\text{Li}$  cells, despite their lower magnetization change compared to Fe/Co systems. However, investigations into the space-charge effect induced by spin-polarized electrons remain unexplored in the realm of HEMs. This gap is particularly critical given HEMs’ unique “cocktail effect” and complex electronic structures endowed by high configurational entropy—including potential, compositionally tunable spin ordering. Understanding how spin-polarized carriers modulate the space-charge layer in HEMs—such as influencing its intensity and distribution, and how this affects charge transfer resistance, interfacial ion diffusion barriers, and interfacial evolution during long-term cycling (*e.g.*, solid/cathode electrolyte interphase formation)—is essential for elucidating

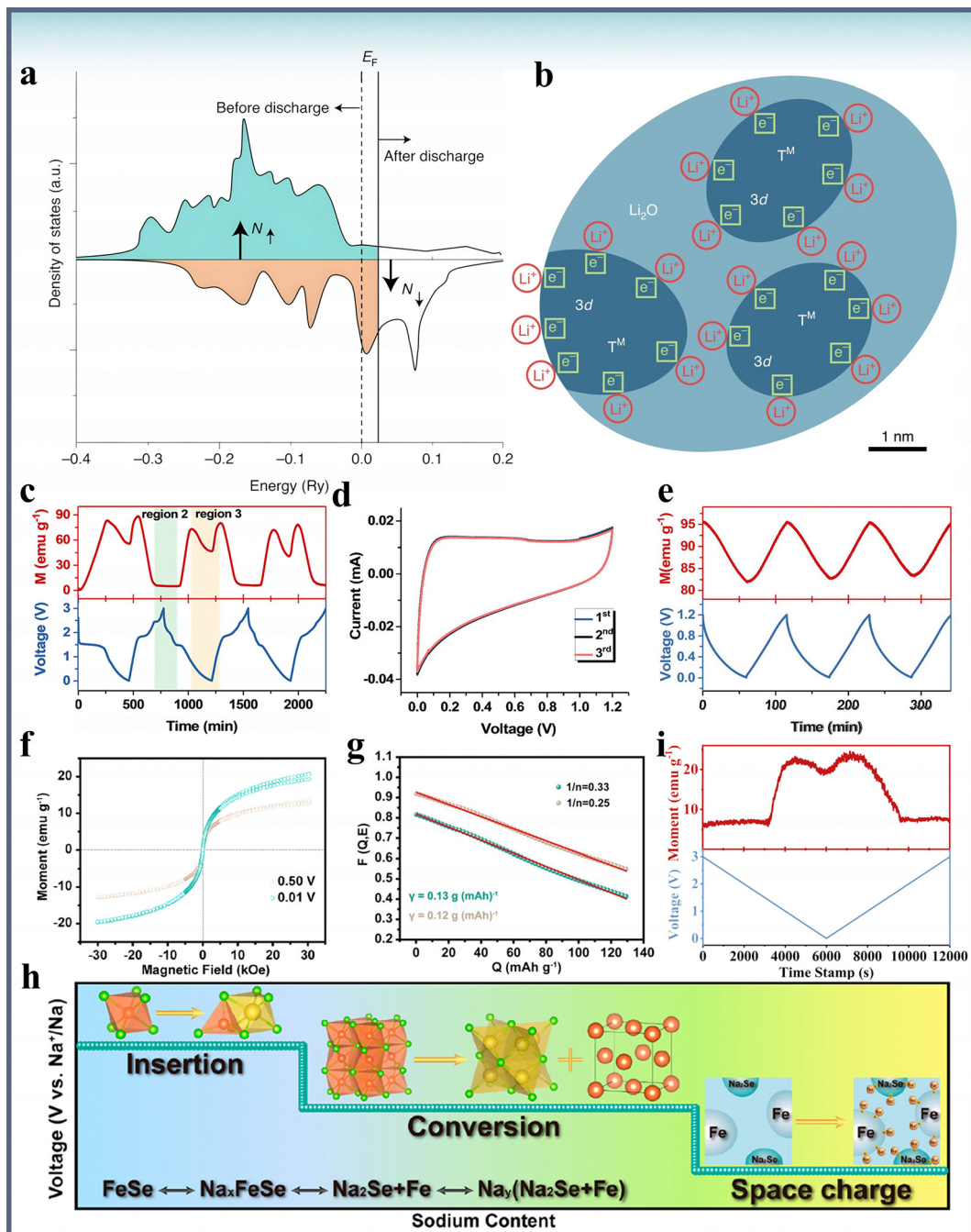


**Fig. 5**  $\text{Fe}_3\text{O}_4/\text{Li}$  cell's (a) schematic of spin-polarized density of states at the surface of ferromagnetic metal grains (before and after discharge), which is opposite to the bulk spin polarization for the case of Fe.  $E_F$ , Fermi energy. (b) Formation of a space-charge zone in the surface capacitance model for extra lithium storage. Reproduced with permission.<sup>57</sup> Copyright 2021, Nature Publishing Group. (c) Time-sequenced *operando* magnetometry and potential response in the first three cycles of  $\text{FeS}_2/\text{Li}$  cells operating at a constant current density of  $200 \text{ mA g}^{-1}$ . (d) CV curves of  $\text{FeS}_2/\text{Li}$  cells for the three cycles at a rate of  $0.5 \text{ mV s}^{-1}$ . (e) function of voltage and magnetization in the three consecutive cycles of discharge-charge from 0 V to 1.2 V. Reproduced with permission.<sup>59</sup> Copyright 2021, American Chemical Society. (f) *Ex situ*  $M$ - $H$  curves for discharging to different voltages at  $0.25 \text{ A g}^{-1}$ , and (g) dependence of  $F(Q, E)$  on interfacial space charge  $Q$  of FeSe nanosheets. (h) Schematic illustration of the sodium storage mechanism of FeSe-NS. Reproduced with permission.<sup>60</sup> Copyright 2023, American Chemical Society. (i) Time-sequenced *operando* magnetometry and potential response in the first cycle of  $\text{NiS}/\text{Li}$  cells.

potential unique electrochemical enhancement mechanisms in HEMs. Therefore, systematic research on the spin-polarized electron-induced space-charge effect in HEMs (especially those with magnetic components or specifically designed electronic

structures) will not only bridge current knowledge gaps but also provide unique perspectives on electronic structure modulation and design principles for developing high-performance HEMs electrodes.

### 3. Element selection and structure design of HEMs

#### 3.1. Element selection

The elemental composition of HEMs directly determines the ion storage mechanism of anodes, thereby influencing their electrochemical performance.<sup>63</sup> Elements that facilitate conversion, alloying, and space charge enhance capacity, while elements that do not participate in conversion contribute to increased cycling stability. Hence, appropriate element selection is crucial for constructing high-performance HEMs with hybrid ion storage mechanisms. Currently, HEM materials used in the anodes of RIBs involve a wide range of cation elements, such as Li, Mg, Al, Si, Ca, Ti, V, Cr, Mn, Fe, Co, Ni, Cu, Zn, Ge, Sr, Mo, Ru, Ag, In, Sn, Sb, La, Ce, W, and Bi, *etc.*, and anion elements, such as P, S, O, Se, and Te, *etc.* However, there is still a lack of systematic summarization of the elements that may occur in different ion storage mechanisms. In this perspective, we comprehensively categorize and summarize the elements potentially involved in distinct ion storage mechanisms. As illustrated in Fig. 6a, to trigger the occurrence of conversion reactions, anion elements like P, S, O, Se, or Te is a prerequisite, while cation elements on Plane A (including Si,<sup>47</sup> Fe,<sup>64</sup> Co,<sup>64</sup> Ni,<sup>64</sup> Cu,<sup>46</sup> Zn,<sup>42</sup> In,<sup>47</sup> Sn,<sup>44</sup> Mn,<sup>65</sup> Ge,<sup>47</sup> Ru,<sup>40</sup> Bi,<sup>44</sup>

Sb,<sup>44</sup> V,<sup>42</sup> and Cr<sup>66</sup>) participate in conversion reactions. It is also important to emphasize that the anion elements significantly govern the feasibility and pathway of conversion reactions in HEMs, as they directly determine the chemical bonding environment, redox activity, and thermodynamic stability of the compound. Furthermore, cation elements on Plane B (including Sn,<sup>44</sup> Bi,<sup>44</sup> Sb,<sup>44</sup> Zn,<sup>67</sup> In,<sup>47</sup> Ge,<sup>47</sup> and Si<sup>47</sup>) after conversion reaction undergo additional alloying reactions, thereby achieving synergistic hierarchical ion storage. Besides, cation elements on Plane C (including Fe,<sup>63,64,68,69</sup> Co,<sup>56,61</sup> and Ni (Fig. 5i)) after conversion reaction can contribute to the space-charge storage, which is beneficial for improving fast-charging performance.

Precise functional selection of elements in HEMs constitutes a core strategy for achieving synergistic enhancement of structural stability and electrochemical performance. In HEM anode systems, the inherent conflict between specific capacity and cycling longevity can be reconciled through coordinated integration of electrochemically active components and inactive structural units. Active cation elements (*e.g.*, Si, Sn, Fe, Co, *etc.*) drive reversible charge storage reactions (including alloying or space-charge mechanisms), directly contributing to capacity. Although certain cation elements (*e.g.*, Li, Mg)—defined as “inactive stabilizers”—primarily function as structural

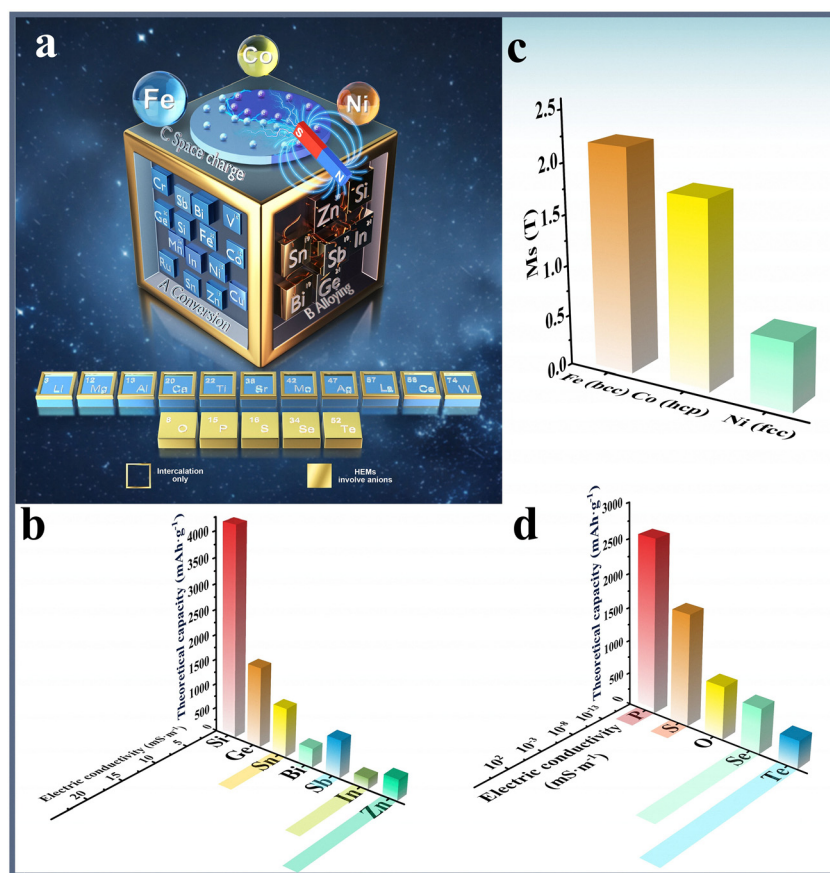


Fig. 6 (a) Research on HEM anodes in RIBs and ion storage mechanisms involving elements. (b) Theoretical specific capacity and intrinsic conductivity of cation elements involved in alloying reactions. (c) Saturation magnetization of Fe, Co, and Ni. (d) Theoretical specific capacity and intrinsic conductivity of HEMs involving anion elements.

stabilizers without participating in conversion reactions. While serving this fundamental structural role, these elements can additionally undergo valence changes that mediate electron transfer, thereby enhancing charge transfer efficiency in pseudocapacitive processes. Concurrently, they function as essential structural pillars, constructing rigid frameworks that alleviate cycling-induced stress and suppress phase separation. It is noteworthy that certain specific elements are not fixed but highly dependent on the overall composition and structure of the material system, meaning that the same element can function either as an active or inactive component in different electrochemical environments. This design principle is convincingly demonstrated in representative studies. For example, in the  $(\text{LiFeZnNiCoMn})_3\text{O}_4$  LIB anode reported by Liu *et al.*,<sup>41</sup> Fe, Co, and Ni enable conversion reactions for capacity delivery, while Li, Zn, and Mn provide essential structural support. The electrode exhibits a capacity retention of 89% after 500 cycles at  $0.5 \text{ A g}^{-1}$ . The high-entropy oxide with a hollow multishelled structure (HEO-HoMS) demonstrates significantly enhanced cycling stability and capacity compared to its unary counterpart. Specifically, the  $(\text{LiFeZnNiCoMn})_3\text{O}_4$  HEO-HoMS maintains 100% of its initial capacity (exceeding  $1200 \text{ mAh g}^{-1}$ ) after 100 cycles at  $0.2 \text{ A g}^{-1}$ , whereas  $\text{Co}_3\text{O}_4$ -HoMS retains only 65% of capacity (final capacity less than  $800 \text{ mAh g}^{-1}$ ) under the same conditions, highlighting the superior structural and electrochemical durability of the high-entropy system. Similarly, in the rock-salt  $(\text{MgCoNiCuZn})\text{O}$  LIB anode developed by Ren *et al.*,<sup>48</sup> Mg functions as a structural stabilizer, whereas Cu, Co, Ni, and Zn participate in conversion reactions to provide primary capacity, with Zn contributing supplementary capacity through additional alloying reactions. This Mg-stabilized HEM anode demonstrates exceptional long-term performance, with almost no capacity decay after 1000 cycles at  $1 \text{ A g}^{-1}$  and a retention of 80% even after 2500 cycles. The two studies highlight the crucial role of electrochemically inactive cation elements in sustaining structural integrity to increase the long cycling stability. The space-charge effect enhances fast-charging stability by enabling spin-polarized interfacial capacitance, as demonstrated by yolk-shell  $\text{FeS/C}$  anodes maintaining 96.8% capacity retention over 10 000 cycles at  $10 \text{ A g}^{-1}$  in the voltage window of the formation of space charge from 0.01 to 1 V.<sup>70</sup> The magnetized interface of superparamagnetic metal nanoparticles significantly promotes stable and rapid ion transport, particularly under high-rate conditions. Therefore, a rational elemental selection strategy is essential to overcome the “capacity-lifespan trade-off” in HEM anodes. Elements that facilitate conversion, alloying, or space-charge mechanisms contribute significantly to high specific capacity and enhanced fast-charging performance, while electrochemically inactive elements improve long-term cycling stability by maintaining structural integrity. Through deliberate combination of these complementary functions, HEMs can simultaneously achieve high capacity, exceptional stability, and superior rate capability.

It is noteworthy that even within a common ion storage mechanism, theoretical specific capacities vary significantly across elements due to differences in atomic mass, number

of electrons transferred, and reaction stoichiometry. For instance, in alloying reactions, Si exhibits a remarkable theoretical capacity of  $4200 \text{ mAh g}^{-1}$ —the highest among all the elements—due to its low atomic weight and ability to host up to 4.4  $\text{Li}^+$  ions (Fig. 6b). However, its extremely low intrinsic electrical conductivity ( $\sim 10^{-5} \text{ S m}^{-1}$ ) severely limits rate performance. In contrast, Ge demonstrates superior rate capability, capable of sustaining ultrafast charging up to  $1000\text{C}$  in architecturally optimized anodes, attributed to its higher intrinsic carrier mobility and ductility, which accommodates rapid ion transport without fracturing.<sup>71</sup> These properties, combined with a high volumetric capacity of  $8646 \text{ mAh cm}^{-3}$ , make nanostructured Ge a promising candidate for high-power applications. This underscores a key advantage of HEMs: the ability to synergistically combine elements with high theoretical capacity and those with high conductivity. Leveraging these intrinsic properties, multi-element synergistic designs have been pursued. A notable example is the ternary medium-entropy compound  $\text{InGeSiP}_3$ , which integrates intercalation, conversion, and alloying mechanisms. Here, Si and Ge provide high Li storage capacity, while In offers high electrical conductivity to facilitate electron transport. These elements act cooperatively, collectively enabling a high reversible capacity of  $1733 \text{ mAh g}^{-1}$ .<sup>47</sup>

The decreasing saturation magnetization from Fe to Co and to Ni (Fig. 6c) leads to reduced efficiency in spin polarization and accumulation of electrons at the interfaces, thus decreasing the capacity contribution from the space-charge effect, sequentially, as discussed in Section 2.4 above. Beyond the role of cations, the selection of anions significantly influences the electrochemical behavior, including both intercalation and conversion processes. While anion elements such as P, S, and O offer high theoretical capacity (Fig. 6d) in such reactions, elements like Se and Te provide distinct practical advantages despite their lower theoretical values. Specifically, Se and Te enhance electronic conductivity and improve reaction kinetics, facilitating more efficient ion intercalation and conversion processes.<sup>44,49</sup> This results in superior rate capability and more effective charge storage, making them particularly suitable for high-power and fast-charging applications. In contrast, P-, S-, and O-based HEMs remain preferable in scenarios where high energy density is the primary requirement.

To support the above viewpoint, we summarize the change of magnetization at key voltage nodes from the electrodes containing superparamagnetic Fe, Co, and Ni conversion. Clearly, a gradual decrease in the extent of magnetization variation of the electrode containing Fe, Co, and Ni conversion during charge-discharge processes is observed in Fig. 7a, thereby weakening the space-charge effect due to Fe, Co, and Ni conversion sequentially. Specifically, the magnetization values at the conversion cutoff voltage, discharge cutoff voltage, and oxidation onset voltage follow the order  $\text{Fe} > \text{Co} > \text{Ni}$  in absolute terms. The differences in magnetization between the conversion cutoff and discharge cutoff voltages, as well as between the oxidation onset and discharge cutoff voltages, also exhibit the same trend ( $\text{Fe} > \text{Co} > \text{Ni}$ ) in relative terms.

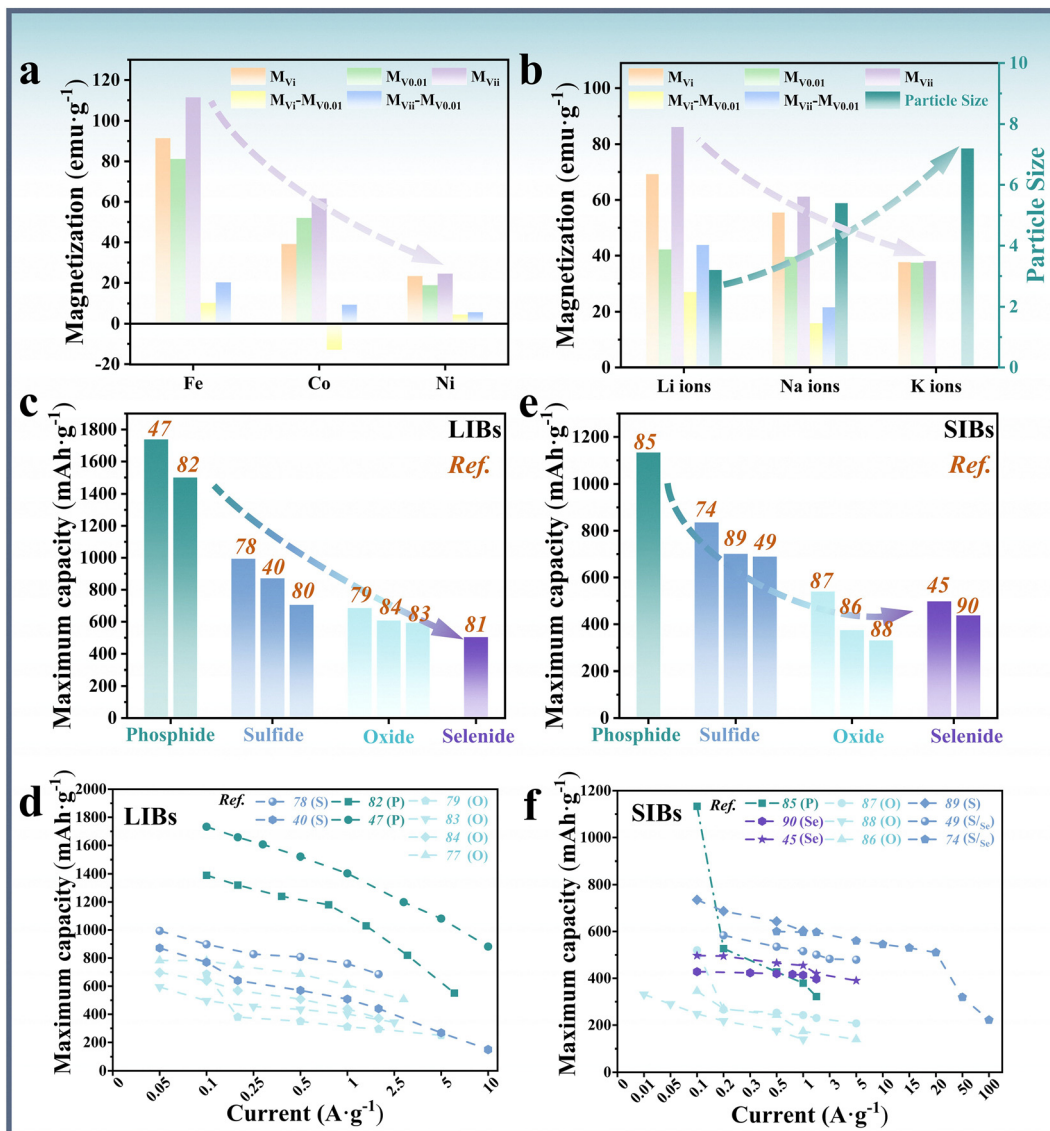


Fig. 7 (a) Summary of changes in electrode magnetization at different voltage nodes induced by the formation of Fe,<sup>67</sup> Co,<sup>56</sup> and Ni nanoparticles during conversion reactions in LIBs. The data on Ni is from Fig. 5i. (b) Summary of changes in electrode magnetization at different voltage nodes induced by the formation of Fe nanoparticles during conversion reactions in LIBs, SIBs, and PIBs.<sup>73</sup> ( $M_{Vi}$ —the value of magnetization corresponds to the conversion cut-off voltage;  $M_{V0.01}$ —the value of magnetization corresponds to the discharge cut-off voltage of 0.01 V;  $M_{Vii}$ —the value of magnetization corresponds to the oxidation onset voltage;  $M_{Vi} - M_{V0.01}$  corresponds to their difference in value;  $M_{Vii} - M_{V0.01}$  corresponds to their difference in value.) (c) and (d) Maximum capacity of different types of representative reported HEMs for (c) LIB and (d) SIB electrodes.<sup>40,45,47,49,74,77-90</sup> (e) and (f) Rate capability of different types of representative reported HEMs for (e) LIB and (f) SIB electrodes.

Notably, for metallic cobalt nanoparticles, an intermediate increase in magnetization is observed between the conversion cutoff and discharge cutoff voltages, which is attributed to the release of internally spin-polarized electrons during this stage.<sup>61</sup> Despite this unique behavior, the overall magnetic variation still follows the sequence Fe > Co > Ni, further indicating that the space-charge effect decreases in the order Fe > Co > Ni, consistent with the experimentally observed differences in practical capacity.<sup>61,72</sup> It is worth noting that even for the same element (taking Fe as an example), systematic differences in magnetization evolution are observed across different alkali-ion systems, as quantitatively compared in

Fig. 7b. Both the absolute magnetization values at characteristic voltages (conversion cutoff, discharge cutoff, and oxidation onset) and the relative changes between these voltages exhibit a consistent decreasing trend: LIB > SIB > PIB, which is attributed to the increasing cation radius from  $\text{Li}^+$  (0.076 nm),  $\text{Na}^+$  (0.102 nm), to  $\text{K}^+$  (0.138 nm). The larger ionic radius decreases intercalation and conversion reaction kinetics, leading to the formation of larger-size conversion products with reduced interfacial area for space-charge layer formation, while simultaneously accommodating fewer charge carriers per unit interface area. This change in magnetization shows a similar trend with the corresponding decline in the strength of the

space-charge effect from lithium-, sodium-, to potassium-ion systems.<sup>73</sup> As shown in Fig. 7c–f, a systematic comparison at different anion systems is conducted on the maximum capacity and rate capability in representative lithium-ion and sodium-ion systems. As illustrated in Fig. 7c, the maximum capacity trends in LIBs align well with theoretical expectations of P, S, O, and Se. In contrast, the corresponding trends for SIBs in Fig. 7d exhibit certain deviations from theoretical predictions, particularly in oxide-based systems. These discrepancies may be attributed to the poor conductivity often associated with oxide materials under sodium cycling conditions, which leads to insufficient sodiation of the active material to prevent the theoretical capacity from being fully utilized. On the contrary, high-conductivity selenides can make the active material more fully sodiated and exert its theoretical capacity, which is more pronounced in SIBs. Therefore, selenides have more advantages as anode materials of SIBs than LIBs. Besides, the rate performance of electrode materials at different anion systems in LIBs and SIBs shows a similar trend with theoretical predictions (electrical conductivity) but still has some deviations (Fig. 7e and f). This is because rate performances are influenced by a combination of multiple factors, including cation selection and structure stability during cycling, *etc.* Among them, selenides exhibit a more excellent rate capability (Fig. 7f) due to high electrical conductivity of Se, whereas phosphides, despite possessing higher theoretical conductivity than oxides, struggle to maintain their high theoretical capacity advantage under high-current charging and discharging conditions due to structural instability caused by large volume expansion. Notably, introducing a small amount of Se into sulfide-based HEMs in SIBs can effectively enhance their conductivity, resulting in significantly improved rate capability compared to pure sulfides (Fig. 7f).<sup>49,74</sup>

To construct practical full cells, HEM anodes have demonstrated excellent compatibility with various commercial cathode materials, as evidenced by several successful configurations. In LIBs, the high-entropy phosphide  $\text{GaCuZnInGeSiP}_6$  pairs effectively with  $\text{LiFePO}_4$ ,<sup>47</sup> while high-entropy oxide  $(\text{LiFeZnNiCoMn})_3\text{O}_4$  couples well with  $\text{LiNi}_{0.8}\text{Co}_{0.1}\text{Mn}_{0.1}\text{O}_2$ .<sup>41</sup> In SIBs, high-entropy sulfide  $\text{Cu}_{0.88}\text{Sn}_{0.02}\text{Sb}_{0.02}\text{Bi}_{0.02}\text{Mn}_{0.02}\text{S}_{0.9}\text{Se}_{0.1}$  works compatibly with  $\text{Na}_3\text{V}_2(\text{PO}_4)_3$ .<sup>49</sup> In PIBs, high-entropy telluride  $\text{Sb}_{1.4}\text{Bi}_{0.2}\text{Sn}_{0.2}\text{Co}_{0.1}\text{Mn}_{0.1}\text{Te}_3$  matches effectively with  $\text{K}_{1.47}\text{Fe}_{0.5}\text{Mn}_{0.5}[\text{Fe}(\text{CN})_6]_{1.26}\text{H}_2\text{O}$ .<sup>44</sup> These diverse pairing examples confirm the practical viability of HEM anodes across multiple battery chemistries.<sup>38,44</sup> However, despite the remarkable electrochemical properties of HEM anodes, including enhanced capacity, cycling stability, and rate capability, a critical challenge remains: their relatively high working voltage, with typical voltage plateaus occurring at  $\sim 1.0$  V compared to conventional anode materials (*e.g.*, graphite or hard carbon operating  $\sim 0.2$  V). This characteristic leads to reduced energy density in full-cell configurations, as the higher working voltage narrows the operational voltage window and consequently lowers the overall voltage output. To fully exploit the potential of HEM anodes in practical applications, future research should focus on strategies to lower their redox potentials while

maintaining structural stability.<sup>47</sup> Possible solutions should focus on incorporating alloying elements with lower working potentials, particularly Si, which exhibits a favorable voltage plateau  $\sim 0.4$  V *versus*  $\text{Li}/\text{Li}^+$  while delivering high specific capacity. Strategic integration of such elements into high-entropy systems presents a promising pathway to reduce the overall operating voltage while maintaining competitive capacity, thereby enhancing the energy density of full-cell configurations.

In addition, the rational selection of constituent elements is equally critical for the successful formation and stabilization of high-entropy phases. For instance, Lun *et al.*<sup>75</sup> computationally evaluated the mixing temperatures of 23 cations in different valence states *via* energy differences between pseudo-random configurations and competing phases, identifying  $\text{Mg}^{2+}$ ,  $\text{Zn}^{2+}$ ,  $\text{Ga}^{3+}$ ,  $\text{Al}^{3+}$ , and  $\text{Sn}^{4+}$  as poorly compatible in conventional systems. However, the ultrahigh configurational entropy in high-entropy environments significantly reduces overall mixing temperatures, enabling the incorporation of otherwise immiscible ions (*e.g.*,  $\text{Cr}^{3+}$ ,  $\text{Sb}^{5+}$ ) into single-phase solid solutions. Furthermore, introducing dual-redox-center cations (*e.g.*,  $\text{Mn}^{2+}/\text{Mn}^{4+}$ ,  $\text{V}^{3+}/\text{V}^{5+}$ ) helps maintain high electron capacity while suppressing undesirable short-range ordering. Lun *et al.*<sup>76</sup> systematically assessed 13 metal cations using metrics such as M–P bond length distribution, intrinsic conductivity, and cost, highlighting that smaller electronegativity differences between phosphorus and metal elements promote weakly polar covalent bonds and facilitate solid-solution formation. Multi-parameter radar chart analysis identifies optimal combinations (*e.g.*,  $\text{Zn–Cu–Sn–Ge–Si–Sb–Fe}$ ) that balance capacity, stability, conductivity, and cost, demonstrating the power of element selection in achieving multifunctional synergy.

### 3.2. Structure design

The selection of elemental components dictates the theoretically accessible ion storage mechanisms—intercalation, conversion, alloying, and space charge. To maximize their collective contributions to capacity, fast-charging capability, and cyclability, a tailored structural design is essential. The overarching principle is to enhance the reaction kinetics of intercalation and conversion, which in turn promotes the formation of finer metal nanoparticles to maximize the alloying and space-charge mechanisms. Lower ion diffusion barriers and higher ion diffusion coefficients facilitate deeper progression of intercalation, which in turn satisfies the thermodynamic conditions required to initiate conversion reactions. This enhances the completeness of conversion (Fig. 8a), refines the particle size of conversion products, and, more importantly, yields finer metallic particulates that alleviate stress concentration from large volume expansion during alloying, thereby mitigating structural collapse (Fig. 8b). Conversely, coarse particles result in incomplete electrochemical reactions, diminished reversibility of conversion processes, and the formation of electrochemically inactive dead zones. Agglomerated nanoparticles further develop thick insulating layers around active materials, severely reducing electronic conductivity, blocking

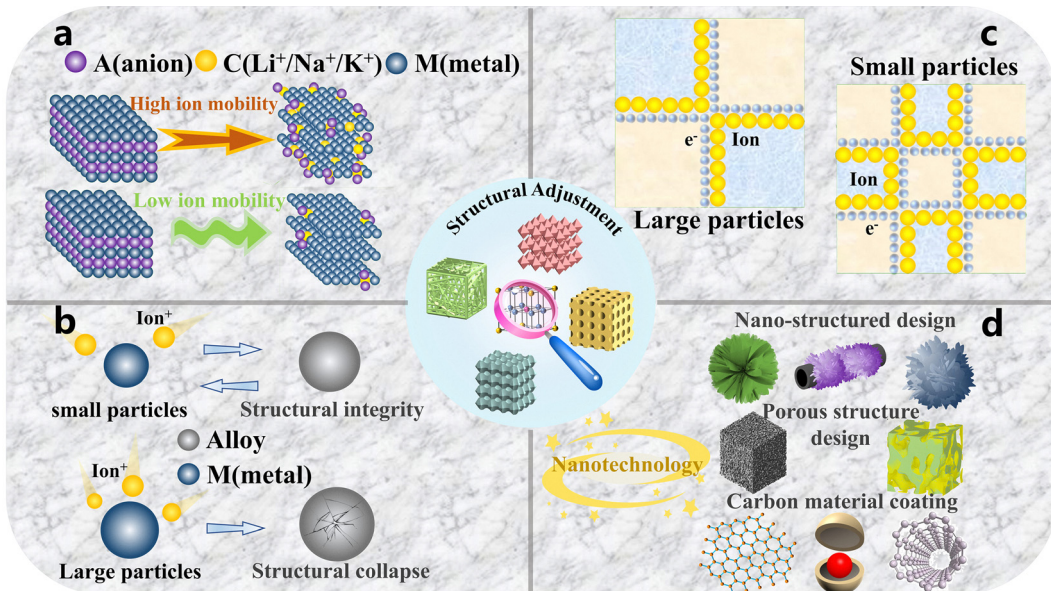


**Fig. 8** Schematic illustrations: (a) the effect of ion types on the extent of conversion reactions. (b) The effect of particle sizes on the structural stability during alloying reactions. (c) The effect of the size of conversion products on the storage number of ions and electrons in the same space. (d) The modified methods of nanostructures.

electron transport to inner regions, and impairing alloying reversibility.<sup>91</sup> The refined metallic particulate size formed during conversion significantly increases the electrochemically active interfacial area available for space-charge storage (Fig. 8c), substantially enhancing the overall capacity of the electrode. Moreover, the presence of metallic particles smaller than 10 nm is essential for enabling a pronounced space-charge effect, with further size reduction enhancing both magnetic properties and space-charge contribution at the interfaces.<sup>57</sup> Ultimately, the effectiveness of structure design in harnessing synergistic contributions from these four mechanisms depends on its ability to modulate two interconnected physicochemical properties: (1) ion diffusion kinetics of intercalation reaction (controlled by diffusion barriers and coefficients), (2) thermodynamics of conversion reactions (determined by Gibbs free energy), which further governs the metallic particle size of conversion products, consequently influencing stress dissipation in alloying reactions and the ion storage interfaces enabled by the space-charge effect.

Strategic structural engineering reduces diffusion barriers and raises diffusion coefficients, promoting intercalation depth and lowering conversion activation energy. This dual action ensures complete conversion and refines metallic nanocrystals. These ultrasmall, stabilized particles favor alloying and maximize space-charge interfaces, collectively unlocking full theoretical capacity. This mechanism was confirmed through *ex situ* XRD and *in situ* TEM experiments by Ren *et al.*<sup>48</sup> Lithiation of HEO ( $\text{MgCoNiCuZn}$ )O led to the irreversible disappearance of the rock-salt phase and the formation of ultrafine metallic nanocomposites. *In situ* nanobattery testing revealed limited volume expansion of only  $\sim 7\%$ —far below the  $> 100\%$  typical of metal oxides—with nearly complete reversal upon delithiation.

No cracking was observed, demonstrating exceptional mechanical resilience and morphology retention, which effectively supports highly reversible alloying behavior. Although research on space-charge effects in HEMs is currently lacking, the principle of regulating the space-charge mechanism in non-high entropy systems can be referenced. For example, Li *et al.*<sup>92</sup> employed a heteroatom doping strategy to engineer Fe-doped MoS<sub>2</sub> anodes for SIBs. This approach precisely tunes the electronic structure and interlayer spacing of layered transition metal sulfides, successfully constructing monolayer Fe-doped MoS<sub>2</sub> that significantly modulates triple ion storage mechanisms: intercalation, conversion, and space charge. The overlapping architecture of monolayer Fe-doped MoS<sub>2</sub> with N,O-co-doped carbon synergistically enhances sodium storage performance through three mechanisms. Expanded interlayer spacing combined with Fe-induced electrostatic repulsion stabilizes the structure, substantially reducing Na<sup>+</sup> diffusion barriers and enabling superior kinetics for intercalation across broad temperature ranges. Spatial confinement by the carbon monolayer suppresses nanocrystal growth during conversion, reducing Mo nanoparticle size from  $\approx 10$  nm in pure MoS<sub>2</sub> electrodes to just over 2 nm—and stabilizing both Mo and Fe particles near  $\sim 2$  nm upon Fe incorporation—which is essential since the spin-polarized surface capacitance effect weakens with increasing size of 3d transition metal nanocrystals and vanishes beyond 10 nm.<sup>57</sup> This not only improves reaction completeness but also shortens ion/electron transport pathways. The overlapping structure of monolayer carbon and MoS<sub>2</sub> suppresses the agglomeration and growth of Fe<sup>0</sup> and Mo<sup>0</sup> nanocrystals generated during the conversion reaction through spatial confinement, stabilizing Fe<sup>0</sup> nanocrystals. Fe<sup>0</sup> nanocrystals are maintained at these critical dimensions, forming charge-

separation zones with  $\text{Na}_2\text{S}$  to generate robust space-charge storage. Particularly in the discharged state, the monolayer configuration significantly increases the  $\text{Fe}/\text{Na}_2\text{S}$  interfacial area<sup>93</sup> (Fig. 8c), substantially boosting  $\text{Na}^+$  storage density in the space-charge region and ultimately doubling the rate capability.

Our recent research found that ion diffusion coefficients and energy barriers in the intercalation reaction, and the Gibbs free energy required for the conversion reaction among Li/Na/K ions show significant differences.<sup>73</sup> This resulted in a decreasing extent of the conversion reaction and contribution of conversion to the specific capacity with the increase of ion radius for LIBs, SIBs, and PIBs (the conversion capacity contributions for SIBs and PIBs were only 90.5% (476.0 mAh g<sup>-1</sup>) and 46.8% (246.1 mAh g<sup>-1</sup>) of that for LIBs (525.9 mAh g<sup>-1</sup>), respectively. This led to substantial differences in the capacity contribution from the space-charge effect (the space-charge capacities for SIBs and PIBs were merely 22.8% (163.0 mAh g<sup>-1</sup>) and 17.1% (122.6 mAh g<sup>-1</sup>) of that for LIBs (714.2 mAh g<sup>-1</sup>), respectively.

HEMs leverage their inherent structural features—lattice distortion, entropy-stabilized effect and sluggish diffusion—to synergistically enhance multi-mechanism energy storage: expanded ion channels facilitate intercalation; flexible frameworks accommodate volume changes during conversion; and gradient bonding, combined with ultrafine metallic particles, effectively dissipates stress in alloying reactions. These structural characteristics collectively contribute to improved reversibility, higher active site availability, and enhanced interfacial ion transport across intercalation, conversion, and alloying processes. For instance, Wei *et al.*<sup>38</sup> investigated the structure-ion storage mechanism relationship in high-entropy Prussian blue analog selenides containing Mn, Co, Ni, Cu, Fe, and Zn. Voids within the high entropy selenide lattice effectively alleviate volume expansion during  $\text{Na}^+$  insertion/extraction, reducing stress concentration. Significant lattice distortion induced by high entropy increases  $\text{Na}^+$  adsorption sites, facilitating easier  $\text{Na}^+$  intercalation and formation of intermediates like  $\text{Na}_x\text{HESe}_2$ . This enhances reversible capacity and kinetic efficiency during intercalation. The high-entropy character effectively suppresses phase separation of multiple elements during reactions, rendering the conversion reaction more completely reversible. These ultrafine metal particles provide abundant electrochemically active sites, significantly reduce charge transfer resistance, and notably weaken lattice expansion from conversion reactions, preserving electrode structural integrity. Conversion reactions occur upon  $\text{Na}^+$  intercalation, generating highly conductive ultrafine metal particles and  $\text{Na}_2\text{Se}$ . No distinct new phases form during conversion; only minor lattice displacement is observed. This stable crystal structure evolution minimizes stress accumulation, ultimately improving the material's structural stability during long-term cycling.

Nanotechnology further enables the construction of low-dimensional and hybrid nanoarchitectures for anodes, providing shortened ion/electron diffusion pathways and enlarged specific surface areas. This significantly accelerates intercalation reaction kinetics while enhancing interfacial-dominant

Table 1 Design guidelines for HEM anodes in LIBs

| Influencing factors               | Ion storage mechanisms  |  |  |                                       |                       |                              |
|-----------------------------------|---|--|--|---------------------------------------|-----------------------|------------------------------|
| Element selection                 | Cations   | Intercalation  | Conversion                             | Alloying                              | Space charge          | Ref.                         |
| Element selection                 | Li, Mg, Al, Si, Ca, Ti, V, Cr, Mn, Fe, Co, Ni, Cu, Zn, Ge, Sr, Mo, Ru, Ag, In, Sn, Sb, La, Ce, W, Bi  | Li, Mg, Al, Si, Ca, Ti, V, Cr, Mn, Fe, Sn, Mn, Ge, Ru, Bi, Sb, V, Cr | Si, Fe, Co, Ni, Cu, Zn, In, Ge, Si     | Sn, Bi, Sb, Zn, In, Ge, Si            | Fe, Co, Ni            | 40, 42, 44, 46, 47 and 64–66 |
| Anions                            | —   | —  | P, S, O, Se, Te<br>P > S > O > Se > Te | —<br>Si > Ge > Sn > Sb > Zn > Bi > In | —<br>Fe > Co > Ni     | 97<br>76 and 98              |
| Theoretical capacity              | —   | —  | Se > Te > P > S > O                    | Si > Ge > Sn > Sb > Zn > Bi > In      | —<br>—<br>↑           | —<br>—<br>↑                  |
| Intrinsic electrical conductivity | —   | —  | —<br>↑                                 | —<br>↑                                | —<br>↑                | —<br>↑                       |
| Structure design                  | Smaller initial particle size<br>Smaller particle size of conversion products<br>Higher conversion product interface density<br>More developed conductive framework<br>Increased defect sites | —<br>—<br>—<br>—<br>—  | —<br>—<br>↑<br>↑<br>↑                  | —<br>—<br>—<br>—<br>↑                 | —<br>—<br>—<br>—<br>— | 47 and 95<br>31 and 41<br>21 |

This upward arrow (↑) indicates that the structural factors have a positive effect on the corresponding ion storage mechanisms.

pseudocapacitive behavior, thereby improving charge/discharge rates. Simultaneously, nanostructures effectively buffer volumetric deformation induced by conversion and alloying reactions, preserving electrode structural integrity and enhancing cycling stability. These features facilitate efficient synergy among multiple ion storage mechanisms (Fig. 8d).<sup>94</sup> Han *et al.*<sup>95</sup> synthesized FeS/C yolk-shell structures featuring hollow carbon layers encapsulating FeS nanosheets, achieving triple synergistic functions. The carbon shell and void space efficiently accommodate volume expansion during sodiation (*in situ* TEM confirms only 4.0% deformation). The carbon coating significantly enhances conductivity and promotes charge transfer. Ultra-small Fe nanoparticles generated upon full sodiation induce strong spin-polarized interfacial capacitance at Fe/Na<sub>2</sub>S interfaces. This effect synchronously enhances ion transport kinetics and contributes additional sodium storage capacity within the low-voltage region (0.01–1 V), particularly excelling at high current densities. Critically, such nanotechnology is equally essential for HEMs, where they provide dual protection under extreme cycling conditions: physical confinement mitigates cyclic stress, while interfacial modification enhances electrode–electrolyte contact and exposes accessible active sites. Wang *et al.*<sup>96</sup> employed phase-separated polymers with distinct decomposition temperatures to fabricate porous hollow HEO nanofibers. This architecture promotes lithium-ion diffusion and accommodates volume expansion, enhancing electrochemical performance in LIBs. During intercalation, the fibrous porous structure provides abundant lithium-ion insertion sites and shortens diffusion paths, while the hollow configuration facilitates rapid electrolyte infiltration, markedly reducing diffusion resistance and boosting intercalation kinetics. This enables more efficient lithium-ion insertion/extraction, increasing the intercalation capacity contribution. During conversion reactions, the porous and hollow fiber matrix effectively buffers volume expansion from metal oxide conversion to metallic species and Li<sub>2</sub>O, preventing material pulverization. Concurrently, the high-entropy effect suppresses metal particle aggregation, ensuring complete and reversible conversion reactions while maintaining conversion capacity stability.

Finally, the crucial roles of elemental selection and structural design in regulating the four primary ion storage mechanisms are summarized. As shown in Table 1, the element selection fundamentally determines which mechanisms are activated: conversion and alloying are driven by electrochemically active cation elements (e.g., Sn, Ge, Si *etc.* for alloying; Fe, Co, Ni for space charge), while structurally stabilizing elements enhance cycling durability. Anionic elements also play a crucial role in determining whether the conversion reaction can occur. Moreover, the intrinsic electrical conductivity and theoretical capacity of the constituent elements govern the rate performance and initial reversible capacity of HEMs to a certain extent. Beyond element selection, tailored structural engineering at multiple scales is essential to fully exploit these mechanisms. Through strategies that minimize primary particle size, construct robust conductive frameworks, and introduce abundant defect sites, we can enhance intercalation and conversion

reaction kinetics. By enhancing intercalation and conversion reaction kinetics, the structural design of HEMs can result in ultrafine metallic nanoparticles and a high density of conversion product interfaces during conversion, such that both alloying efficiency and space-charge storage are significantly enhanced.

## 4. Conclusion and perspective

In summary, HEMs can effectively integrate four ion storage mechanisms—intercalation, conversion, alloying, and space charge—through multi-element synergy, offering a promising strategy to overcome the capacity-rate-cycling trade-offs of conventional anodes in RIBs. The selection of elements fundamentally determines which mechanisms are activated: conversion and alloying are driven by electrochemically active cation elements (e.g., Sn, Ge, Si *etc.* for alloying; Fe, Co, Ni for space charge), while structurally stabilizing elements enhance cycling durability. Anion elements also play a critical role; for instance, Se has a high conductivity to benefit the improvement of rate performance of HEMs; P and S have high theoretical capacities after binding with alkali metal ions, which can improve the reversible capacity of HEMs. Beyond element selection, tailored structural engineering at multiple scales is essential to fully exploit these mechanisms. By enhancing intercalation and conversion kinetics, HEMs promote the formation of ultrafine metallic nanoparticles that facilitate efficient alloying and amplify space-charge storage. This synergistic approach—combining element selection with hierarchical structure design—enables simultaneous improvements in capacity, cycling life, and fast-charging performance. Moving forward, elucidating the interplay of multi-ion storage mechanisms, especially the underexplored space-charge effect, and advancing synthetically scalable architectures will be key to unlocking the full potential of HEM anodes for next-generation RIBs.

However, research on HEM ion storage mechanisms and optimized design remains at a nascent stage. The complexity introduced by multi-component systems (elements/solvents/salts) poses significant challenges to elucidating intrinsic mechanisms. A universal theoretical framework for systematically interpreting HEM functionality evolution is still lacking. Consequently, three critical breakthroughs are required for HEMs' anodes in the RIBs. An integrated summary of ion storage mechanisms and three key research frontiers in HEM anodes is presented in Fig. 9.

(I) The super-exponential combinatorial space and near-infinite property distributions in HEMs with five or more components induce a dimensionality catastrophe for traditional trial-and-error approaches. Manual screening proves inefficient due to the strong sensitivity of synthesis routes and parameters (temperature/pressure/precursor ratios, *etc.*) to microstructures, phase composition, and defect concentration. Identical compositions can yield divergent morphologies (nanodendrites, porous frameworks, core–shell structures, *etc.*), amplifying performance prediction complexity. To resolve this multidimensional

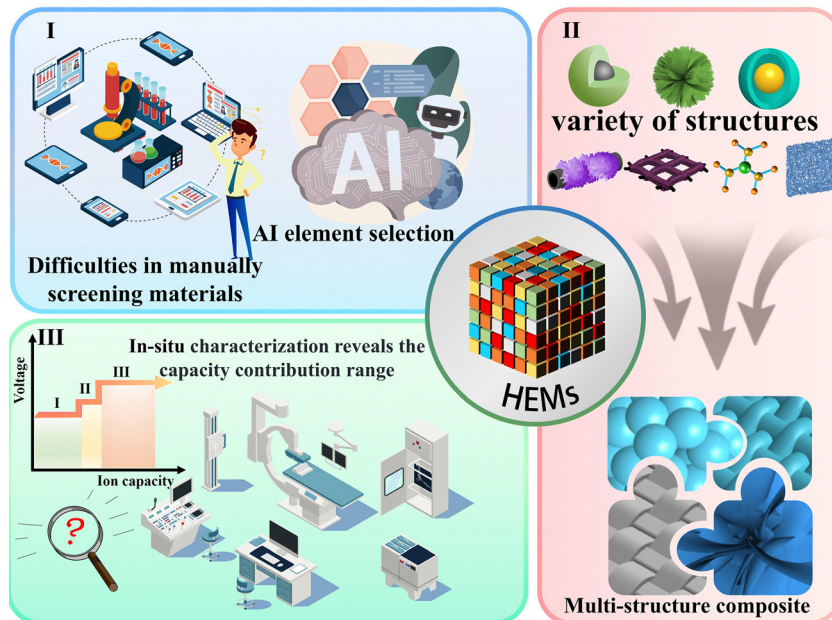


Fig. 9 Three breakthrough dimensions in HEMs anodes: (I) intelligent design, (II) structural innovation and (III) mechanism elucidation.

coupling challenge, an AI-driven paradigm shift is imperative: establishing a cross-scale digital twin platform *via* generative large models, decoding implicit process–structure–property relationships through deep neural networks. Integrating high-throughput quantum computing for entropy-stable phase screening enables precise targeting of materials with desired properties from vast “composition–process–structure” combinations, revolutionizing experience-oriented material development.

(II) To meet the stringent commercial requirements for energy storage—including high initial coulombic efficiency, high capacity, long cyclability, and excellent rate capability—a fundamental breakthrough through deliberate multiscale structural design is imperative. While HEMs offer unique compositional advantages, their structural configuration remains underexplored and represents a critical direction for future development. To maximize the synergy of the four primary storage mechanisms—intercalation, conversion, alloying, and space-charge storage—structural optimization must occur across multiple scales: at the atomic scale, precise structural design can greatly improve storage kinetics: Single-atom dispersion or sub-nanometric clusters significantly increase active sites and shorten diffusion lengths, thereby enhancing ion diffusion kinetics; tailored cationic valence gradients reconstruct continuous conductive networks to facilitate charge transfer; rational anion selection adjusts ligand fields to reduce diffusion energy barriers, promoting rapid ion transport. These designs are beneficial for the intercalation reaction. At the nanoscale, interface and morphology engineering play decisive roles: core–shell interfaces by compositing highly conductive carbon materials with HEMs accelerate charge transport and structure stability; yolk–shell or porous structure by finely controlled porosity not only buffers large volume variation in conversion and alloying reactions but also ensures efficient ion

flux and structural integrity. Beyond intrinsic material design, further performance enhancement can be achieved through integration with exogenous structural systems, such as supported matrix materials (carbon nanofibers, nanotubes, and felts, *etc.*), which improve electrical connectivity and alleviate mechanical degradation during cycling. This kind of holistic and multi-level structural strategy is expected to promote HEM-based anodes to approach theoretical limits of initial Coulombic efficiency, second-level rate performance, and ultra-long cycle life, thereby accelerating their commercialization.

(III) The electrochemical performance of HEMs is attributed to multi-mechanism synergy, yet fundamental challenges persist regarding the voltage-resolved activity and quantitative capacity contribution of each ion storage mechanism. Conventional *ex situ* characterization techniques offer limited insight into dynamic and coupled processes of the four mechanisms, particularly under realistic operating conditions. In addition, the synergy of the four mechanisms involves a series of complex processes, such as the interaction between spin-polarized electrons and transition metals, the interaction between electric and magnetic fields, and the mutual conversion between electrical and chemical energy. It is difficult to solve the challenges using a single *in situ* characterization technique. A combination of multiple advanced *in situ* characterization techniques is expected to overcome this challenge. For example, *in situ* XRD enables real-time tracking of phase transitions and lattice evolution of intercalation, conversion and alloying reactions. *In situ* TEM provides nanoscale visualization of structural revolution, including the process of conversion and alloying reactions. *Operando* magnetometry detects conversion onset and end voltages, spin-polarized electron transfer and the corresponding magnetic responses during space-charge storage. *In situ* EIS and EPR spectroscopy offer complementary

insights into charge transfer kinetics and electron structure evolution during the four ion storage mechanisms. Together, these techniques form a multidimensional platform for deciphering mechanism-specific potentials, quantifying individual capacity contributions, and ultimately establishing a mechanistic foundation for the rational design of HEM electrodes with tailored ion storage behavior.

## Conflicts of interest

The authors declare no competing financial interest.

## Data availability

Data sharing is not applicable to this article as no new data were created or analyzed in this study. All data necessary to support the findings of this study are available within the main text and the cited references.

## Acknowledgements

This perspective was financially supported by the Shenzhen Science and Technology Program (No. JCYJ20240813094208011), the National Natural Science Foundation of China (No. 22309076), the Shenzhen Key Laboratory of Advanced Energy Storage (No. ZDSYS2022040114100001), and the High level of special funds (No. G03034K001).

## References

- W. Yao, K. Liao, T. Lai, H. Sul and A. Manthiram, *Chem. Rev.*, 2024, **124**, 4935–5118.
- Y. Wang, X. Yang, Y. Meng, Z. Wen, R. Han, X. Hu, B. Sun, F. Kang, B. Li, D. Zhou, C. Wang and G. Wang, *Chem. Rev.*, 2024, **124**, 3494–3589.
- Y. Ding, Z. P. Cano, A. Yu, J. Lu and Z. Chen, *Electrochem. Energy Rev.*, 2019, **2**, 1–28.
- M. Á. Muñoz-Márquez, D. Saurel, J. L. Gómez-Cámer, M. Casas-Cabanas, E. Castillo-Martínez and T. Rojo, *Adv. Energy Mater.*, 2017, **7**, 1700463.
- X. Deng, L. Li, G. Zhang, X. Zhao, J. Hao, C. Han and B. Li, *Energy Storage Mater.*, 2022, **53**, 467–481.
- T. Hosaka, K. Kubota, A. S. Hameed and S. Komaba, *Chem. Rev.*, 2020, **120**, 6358–6466.
- D. Li, Y. Yuan, J. Liu, M. Fichtner and F. Pan, *J. Magnes. Alloys*, 2020, **8**, 963–979.
- T. Perveen, M. Siddiq, N. Shahzad, R. Ihsan, A. Ahmad and M. I. Shahzad, *Renewable Sustainable Energy Rev.*, 2020, **119**, 109549.
- A. Kumar Prajapati and A. Bhatnagar, *J. Energy Chem.*, 2023, **83**, 509–540.
- J. Maier, *Faraday Discuss.*, 2006, **134**, 51–66.
- J.-S. Lee, S. Tai Kim, R. Cao, N.-S. Choi, M. Liu, K. T. Lee and J. Cho, *Adv. Energy Mater.*, 2011, **1**, 34–50.
- N. Nitta, F. Wu, J. T. Lee and G. Yushin, *Mater. Today*, 2015, **18**, 252–264.
- F. Wu, J. Maier and Y. Yu, *Chem. Soc. Rev.*, 2020, **49**, 1569–1614.
- Y. Xu, E. Swaans, S. Basak, H. W. Zandbergen, D. M. Borsa and F. M. Mulder, *Adv. Energy Mater.*, 2016, **6**, 1501436.
- J. Jamnik and J. Maier, *Phys. Chem. Chem. Phys.*, 2003, **5**, 5215–5220.
- J. Maier, *Faraday Discuss.*, 2007, **134**, 51–66.
- B. Cantor, I. T. H. Chang, P. Knight and A. J. B. Vincent, *Mater. Sci. Eng. A*, 2004, **375**, 213–218.
- J.-W. Yeh, S.-K. Chen, S.-J. Lin, J.-Y. Gan, T.-S. Chin, T.-T. Shun, C.-H. Tsau and S.-Y. Chang, *Adv. Eng. Mater.*, 2004, **6**, 299–303.
- B. Ouyang and Y. Zeng, *Nat. Commun.*, 2024, **15**, 973.
- K.-H. Tian, C.-Q. Duan, Q. Ma, X.-L. Li, Z.-Y. Wang, H.-Y. Sun, S.-H. Luo, D. Wang and Y.-G. Liu, *Rare Met.*, 2021, **41**, 1265–1275.
- W. Yin, X. Nie, X. Shi, J. Wang and Z. Sun, *J. Power Sources*, 2025, **629**, 236021.
- D. Lai, Q. Kang, F. Gao and Q. Lu, *J. Mater. Chem. A*, 2021, **9**, 17913–17922.
- Z.-Y. Gu, J.-Z. Guo, J.-M. Cao, X.-T. Wang, X.-X. Zhao, X.-Y. Zheng, W.-H. Li, Z.-H. Sun, H.-J. Liang and X.-L. Wu, *Adv. Mater.*, 2022, **34**, 2110108.
- S. Li, H. Peng, L. Tong, Y. Xie, B. Zhang and X. Fu, *Acta Mater.*, 2025, **287**, 120813.
- M. Rouholamini, C. Wang, H. Nehrir, X. Hu, Z. Hu, H. Aki, B. Zhao, Z. Miao and K. Strunz, *IEEE Trans. Smart Grid*, 2022, **13**, 4505–4524.
- G. Qiu, T. Li, X. Xu, Y. Liu, M. Niyogi, K. Cariaga and C. Oses, *npj Comput. Mater.*, 2025, **11**, 145.
- C. Oses, C. Toher and S. Curtarolo, *Nat. Rev. Mater.*, 2020, **5**, 295–309.
- N. Kar and S. E. Skrabalak, *Nat. Rev. Mater.*, 2025, **10**, 638–653.
- W. Ye, F. Wu, N. Shi, H. Zhou, Q. Chi, W. Chen, S. Du, P. Gao, H. Li and S. Xiong, *Small*, 2020, **16**, 1906607.
- A. J. Jacobson and L. F. Nazar, *Intercalation Chemistry, Encyclopedia of Inorganic and Bioinorganic Chemistry*, 2011.
- C.-Y. Huang, C.-W. Huang, M.-C. Wu, J. Patra, T. Xuyen Nguyen, M.-T. Chang, O. Clemens, J.-M. Ting, J. Li, J.-K. Chang and W.-W. Wu, *Chem. Eng. J.*, 2021, **420**, 129838.
- J. Zhao, Y. Zhang, X. Chen, G. Sun, X. Yang, Y. Zeng, R. Tian and F. Du, *Adv. Funct. Mater.*, 2022, **32**, 2206531.
- P.-W. Chien, C.-B. Chang and H.-Y. Tuan, *Energy Storage Mater.*, 2023, **61**, 102853.
- X. Lei, Y. Wang, J. Wang, Y. Su, P. Ji, X. Liu, S. Guo, X. Wang, Q. Hu, L. Gu, Y. Zhang, R. Yang, G. Zhou and D. Su, *Small Methods*, 2024, **8**, 2300754.
- B. Xiao, G. Wu, T. Wang, Z. Wei, Y. Sui, B. Shen, J. Qi, F. Wei and J. Zheng, *Nano Energy*, 2022, **95**, 106962.
- K. Wang, W. Hua, X. Huang, D. Stenzel, J. Wang, Z. Ding, Y. Cui, Q. Wang, H. Ehrenberg, B. Breitung, C. Kübel and X. Mu, *Nat. Commun.*, 2023, **14**, 1487.

37 W. Li, J.-H. Wang, Y. Li, H. Hsueh, X. Liu, Y. Zhao, S. Huang, X. Li, H.-M. Cheng, X. Duan and H. S. Park, *J. Am. Chem. Soc.*, 2024, **146**, 21320–21334.

38 C. Wei, C. Li, D. Qu, B. Liao, D. Han, Z.-H. Sun and L. Niu, *J. Colloid Interface Sci.*, 2024, **675**, 139–149.

39 C. Roberto, G. Nadia, V. Daniele, A. Julia, P. M. Laura, Q. Eliana, F. Carlotta, B. Federico and B. Silvia, *J. Mater. Sci.*, 2022, **57**, 15690–15704.

40 W. Cheng, J. Liu, J. Hu, W. Peng, G. Niu, J. Li, Y. Cheng, X. Feng, L. Fang, M.-S. Wang, S. A. T. Redfern, M. Tang, G. Wang and H. Gou, *Small*, 2023, **19**, 2301915.

41 X. Liu, Y. Yu, K. Li, Y. Li, X. Li, Z. Yuan, H. Li, H. Zhang, M. Gong, W. Xia, Y. Deng and W. Lei, *Adv. Mater.*, 2024, **36**, 2312583.

42 S. Hou, L. Su, S. Wang, Y. Cui, J. Cao, H. Min, J. Bao, Y. Shen, Q. Zhang, Z. Sun, C. Zhu, J. Chen, Q. Zhang and F. Xu, *Adv. Funct. Mater.*, 2024, **34**, 2307923.

43 W. Bian, H. Li, Z. Zhao, H. Dou, X. Cheng and X. Wang, *Electrochim. Acta*, 2023, **447**, 142157.

44 Z. Wang, S. Qiao, M. Ma, T. Li, H. K. Liu, S. X. Dou and S. Chong, *ACS Nano*, 2025, **19**, 15148–15160.

45 D.-Y. Qu, Q.-Y. Li, Z.-H. Sun, C.-Y. Wei, Z.-Y. Gu, X.-X. Zhao, B.-L. Zhao, D.-X. Han, L. Niu and X.-L. Wu, *Adv. Funct. Mater.*, 2024, **35**, 2421504.

46 O. J. Marques, C. Chen, E. V. Timofeeva and C. U. Segre, *J. Power Sources*, 2023, **564**, 232852.

47 W. Li, J.-H. Wang, L. Yang, Y. Li, H.-Y. Yen, J. Chen, L. He, Z. Liu, P. Yang, Z. Guo and M. Liu, *Adv. Mater.*, 2024, **36**, 2314054.

48 R. Ren, Y. Xiong, Z. Xu, J. Zhang, Y. Zhang, G. Zhu, K. Yin and S. Dong, *Chem. Eng. J.*, 2024, **479**, 147896.

49 S. Zhang, W. Zuo, X. Fu, J. Li, Q. Zhang, W. Yang, H. Chen, J. Zhang, X. Xiao, K. Amine, S.-G. Sun, F. Fu, M. Ye and G.-L. Xu, *Nat. Commun.*, 2025, **16**, 4052.

50 Y. Jia, S. Chen, X. Shao, J. Chen, D.-L. Fang, S. Li, A. Mao and C. Li, *J. Adv. Ceram.*, 2023, **12**, 1214–1227.

51 T. X. Nguyen, C.-C. Tsai, J. Patra, O. Clemens, J.-K. Chang and J.-M. Ting, *Chem. Eng. J.*, 2022, **430**, 132658.

52 K.-H. Tian, C.-Q. Duan, Q. Ma, X.-L. Li, Z.-Y. Wang, H.-Y. Sun, S.-H. Luo, D. Wang and Y.-G. Liu, *Rare Met.*, 2022, **41**, 1265–1275.

53 Y.-Y. Hu, Z. Liu, K.-W. Nam, O. J. Borkiewicz, J. Cheng, X. Hua, M. T. Dunstan, X. Yu, K. M. Wiaderek, L.-S. Du, K. W. Chapman, P. J. Chupas, X.-Q. Yang and C. P. Grey, *Nat. Mater.*, 2013, **12**, 1130–1136.

54 S. Laruelle, S. Grugeon, P. Poizot, M. Dolle, L. Dupont and J. Tarascon, *J. Electrochem. Soc.*, 2002, **149**, A627.

55 L. Fu, C.-C. Chen and J. Maier, *Solid State Ionics*, 2018, **318**, 54–59.

56 T. Meyer, T. Gutel, H. Manzanarez, T. Genieys, J. Almoric, M. Bardet and E. De Vito, *ACS Appl. Energy Mater.*, 2024, **7**, 9939–9952.

57 Q. Li, H. Li, Q. Xia, Z. Hu, Y. Zhu, S. Yan, C. Ge, Q. Zhang, X. Wang, X. Shang, S. Fan, Y. Long, L. Gu, G.-X. Miao, G. Yu and J. S. Moodera, *Nat. Mater.*, 2021, **20**, 76–83.

58 C.-G. Duan, J. P. Velev, R. F. Sabirianov, Z. Zhu, J. Chu, S. S. Jaswal and E. Y. Tsymbal, *Phys. Rev. Lett.*, 2008, **101**, 137201.

59 Z. Li, Y. Zhang, X. Li, F. Gu, L. Zhang, H. Liu, Q. Xia, Q. Li, W. Ye, C. Ge, H. Li, H. Hu, S. Li, Y.-Z. Long, S. Yan, G.-X. Miao and Q. Li, *J. Am. Chem. Soc.*, 2021, **143**, 12800–12808.

60 D. Qiu, A. Gao, W. Zhao, Z. Sun, B. Zhang, J. Xu, T. Shen, J. Wang, Z. Fang and Y. Hou, *ACS Energy Lett.*, 2023, **8**, 4052–4060.

61 F. Zuo, H. Zhang, Y. Ding, Y. Liu, Y. Li, H. Liu, F. Gu, Q. Li, Y. Wang, Y. Zhu, H. Li and G. Yu, *Proc. Natl. Acad. Sci. U. S. A.*, 2023, **120**, e2314362120.

62 H. Li, Z. Hu, F. Zuo, Y. Li, M. Liu, H. Liu, Y. Li, Q. Li, Y. Ding, Y. Wang, Y. Zhu, G. Yu and J. Maier, *Proc. Natl. Acad. Sci. U. S. A.*, 2024, **121**, e2320030121.

63 C. Du, Z. Zhao, H. Liu, F. Song, L. Chen, Y. Cheng and Z. Guo, *Chem. Rec.*, 2023, **23**, e202300004.

64 C. Triolo, M. Maisuradze, M. Li, Y. Liu, A. Ponti, G. Pagot, V. Di Noto, G. Aquilanti, N. Pinna, M. Giorgetti and S. Santangelo, *Small*, 2023, **19**, 2304585.

65 X. Liu, L. Ding, K. Li, J. Lv, J. Wen, H. Zhang, Y. Wang, Y. Yao and W. Lei, *Acta Mater.*, 2025, **287**, 120812.

66 H. K. Beere, N. S. Reddy, P. Kulkarni, K. Samanta, H. Y. Jung and D. Ghosh, *J. Energy Storage*, 2024, **80**, 110325.

67 X. Li, J.-H. Wang, L. Yang, T.-Y. Liu, S. Huang, B. Ho, H. Hsueh, J. Chen, L. He, Z. Guo, M. Liu and W. Li, *Adv. Mater.*, 2024, **36**, 2409278.

68 J. Liu, K. Zheng, Y. Mu, Z. Zou, M. Han, C. Deng, J. Guo, F. Yu, W. Li, L. Wei, L. Zeng and T. Zhao, *Nano Energy*, 2024, **131**, 110266.

69 M. Han, K. Zheng, J. Liu, Z. Zou, Y. Mu, H. Hu, F. Yu, W. Li, L. Wei, L. Zeng and T. Zhao, *J. Mater. Chem. A*, 2025, **13**, 1086–1094.

70 M. Han, J. Liu, C. Deng, J. Guo, Y. Mu, Z. Zou, K. Zheng, F. Yu, Q. Li, L. Wei, L. Zeng and T. Zhao, *Adv. Energy Mater.*, 2024, **14**, 2400246.

71 M. Han, Z. Zou, J. Liu, C. Deng, Y. Chu, Y. Mu, K. Zheng, F. Yu, L. Wei, L. Zeng and T. Zhao, *Small*, 2024, **20**, 2312119.

72 Q. Li, H. Li, Q. Xia, Z. Hu, Y. Zhu, S. Yan, C. Ge, Q. Zhang, X. Wang, X. Shang, S. Fan, Y. Long, L. Gu, G.-X. Miao, G. Yu and J. S. Moodera, *Nat. Mater.*, 2020, **20**, 76–83.

73 K. Zheng, Y. Mu, M. Han, J. Liu, Z. Zou, H. Hu, Y. Chu, F. Yu, W. Li, L. Wei, L. Zeng and T. Zhao, *Adv. Sci.*, 2024, **11**, 2410653.

74 X. Nie, Z. Chen, B. Deng, L. Shao, J. Xu, X. Shi and Z. Sun, *Adv. Energy Mater.*, 2025, **15**, 2500069.

75 Z. Lun, B. Ouyang, D.-H. Kwon, Y. Ha, E. E. Foley, T.-Y. Huang, Z. Cai, H. Kim, M. Balasubramanian, Y. Sun, J. Huang, Y. Tian, H. Kim, B. D. McCloskey, W. Yang, R. J. Clément, H. Ji and G. Ceder, *Nat. Mater.*, 2021, **20**, 214–221.

76 Y. Liu, C. Zeng, X. Liu, X. Wei, X. Ji, Q. Zha, G. Du, X. Zhong, X. Liu, T. Zhai and H. Li, *Adv. Funct. Mater.*, 2025, e10753.

77 T. X. Nguyen, J. Patra, C.-C. Tsai, W.-Y. Xuan, H.-Y. T. Chen, M. S. Dyer, O. Clemens, J. Li, S. B. Majumder, J.-K. Chang and J.-M. Ting, *Adv. Funct. Mater.*, 2023, **33**, 2300509.

78 L. Lin, K. Wang, A. Sarkar, C. Njel, G. Karkera, Q. Wang, R. Azmi, M. Fichtner, H. Hahn, S. Schweidler and B. Breitung, *Adv. Energy Mater.*, 2022, **12**, 2103090.

79 L. Su, J. Ren, T. Lu, K. Chen, J. Ouyang, Y. Zhang, X. Zhu, L. Wang, H. Min, W. Luo, Z. Sun, Q. Zhang, Y. Wu, L. Sun, L. Mai and F. Xu, *Adv. Mater.*, 2023, **35**, 2205751.

80 Q. An, S. Li, J. Zhou, S. Ji, Z. Wen and J. Sun, *Adv. Eng. Mater.*, 2023, **25**, 2300585.

81 S. A. Alvi, A. Black Serra, I. S. Jozami, F. Akhtar and P. Johansson, *ECS Meeting Abstracts*, 2023, 648.

82 Y. Wei, R. Yao, X. Liu, W. Chen, J. Qian, Y. Yin, D. Li and Y. Chen, *Adv. Sci.*, 2023, **10**, 2300271.

83 T.-Y. Chen, S.-Y. Wang, C.-H. Kuo, S.-C. Huang, M.-H. Lin, C.-H. Li, H.-Y. T. Chen, C.-C. Wang, Y.-F. Liao, C.-C. Lin, Y.-M. Chang, J.-W. Yeh, S.-J. Lin, T.-Y. Chen and H.-Y. Chen, *J. Mater. Chem. A*, 2020, **8**, 21756–21770.

84 S. Mu, Z. Liu, K. Wang, H. Shi, M. Zhou, F. Wang, Z. Ni and C. Yuan, *J. Power Sources*, 2025, **625**, 235603.

85 H. Li, Y. Duan, Z. Zhao, X. Cheng, W. Bian, Z. Xiao and X. Wang, *Chem. Eng. J.*, 2023, **469**, 143951.

86 H. Xu, H. Li, M. Gao, W. Yi, Z. Zhao and X. Wang, *J. Energy Storage*, 2025, **113**, 115641.

87 B. Xiao, X. Liu, Z. Xie, D. Zheng, J. Zha, J. Qi, F. Wei, Q. Meng, X. Xue, D. Zhao, Y. Li, Q. Yin, L. Ma, M. Ge, X. Xiao, Y. Sui, S. Chen and J. Zheng, *Chem. Eng. J.*, 2025, **503**, 158269.

88 X. Nie, Z. Chen, B. Deng, L. Shao, J. Xu, X. Shi and Z. Sun, *Adv. Energy Mater.*, 2025, **15**, 2500069.

89 M. Chen, Y. Liu, Z. Fang, Y. Wang, S. Gu and G. Zhou, *Nanomaterials*, 2025, **15**, 881.

90 Y. Zhang, J. y Xing, M. Chen and Q. Jin, *Chem. Eng. J.*, 2023, **479**, 147709.

91 L. Fang, N. Bahlawane, W. Sun, H. Pan, B. B. Xu, M. Yan and Y. Jiang, *Small*, 2021, **17**, 2101137.

92 Z. Li, M. Han, J. Wang, L. Zhang, P. Yu, Q. Li, X. Bai and J. Yu, *Adv. Funct. Mater.*, 2024, **34**, 2404263.

93 C.-C. Chen and J. Maier, *Nat. Energy*, 2018, **3**, 102–108.

94 A. Bhatnagar, M. Tripathi and A. Prajapati, *Nanotechnology for Electronic Applications*, 2022, pp. 29–48.

95 M. Han, J. Liu, C. Deng, J. Guo, Y. Mu, Z. Zou, K. Zheng, F. Yu, Q. Li, L. Wei, L. Zeng and T. Zhao, *Adv. Energy Mater.*, 2024, **14**, 2400246.

96 X. L. Wang, E. M. Kim, T. G. Senthamaraiannan, D.-H. Lim and S. M. Jeong, *Chem. Eng. J.*, 2024, **484**, 149509.

97 C. Li, X. Chen, J. Li, Y. Xiang, Y. Yao, W. Liao, W. Xue, X. Zhang and Y. Xiang, *Energy Storage Mater.*, 2024, **71**, 103468.

98 H. Nguyen and R. J. Clément, *ACS Energy Lett.*, 2020, **5**, 3848–3859.